Multidimensional Femtosecond Correlation Spectroscopies of Electronic and Vibrational Excitations

Shaul Mukamel

Department of Chemistry and Rochester Theory Center for Optical Science and Engineering, University of Rochester, PO Box 270216, Rochester, New York 14627-0216; e-mail: Mukamel@chem.Rochester.edu

■ **Abstract**   Femtosecond visible and infrared analogues of multiple-pulse nuclear magnetic resonance techniques provide novel snapshot probes into the structure and electronic and vibrational dynamics of complex molecular assemblies such as photosynthetic antennae, proteins, and hydrogen-bonded liquids. A classical-oscillator description of these spectroscopies in terms of interacting quasiparticles (rather than transitions among global eigenstates) is developed and sets the stage for designing new pulse sequences and inverting the multidimensional signals to yield molecular structures. Considerable computational advantages and a clear physical insight into the origin of the response and the relevant coherence sizes are provided by a real-space analysis of the underlying coherence-transfer pathways in Liouville space.

INTRODUCTION

Spectroscopic techniques based on the application of sequences of carefully shaped and timed femtosecond pulses provide a novel multidimensional view of molecular structure as well as vibrational and electronic motions, interactions, and relaxation processes (1, 2). Conventional spectroscopies such as linear absorption and spontaneous and coherent Raman give a one-dimensional (1D) projection of molecular interactions onto a single-frequency (or time) axis. For simple molecules with well-separated eigenstates this provides direct information on energy levels and their oscillator strengths. The situation is different in complex molecules with strongly congested levels. Here the microscopic information is highly averaged and is often totally buried under broad, featureless line shapes, whose precise interpretation remains a mystery.

   Recent advances in pulse-shaping techniques (3–10a) make it possible to vary the envelopes, polarization directions, durations, and time intervals, to tune the

frequencies, and even to control the phases of optical pulses. By scanning these various parameters it is possible to custom design a multiple-pulse technique for a specific application (as is routinely done in nuclear magnetic resonance NMR) (11–13). Displaying the signal obtained by varying n parameters results in n-dimensional correlation plots, which form the basis of nD spectroscopies. One option is to vary n time-intervals between short pulses, but any other choice of parameters is possible. Spreading the spectroscopic information in more than one dimension helps resolve congested spectra, selectively eliminates certain static broadening mechanisms, and provides ultrafast structural and dynamical information unavailable from 1D measurements.

Multidimensional spectroscopies provide a wealth of information. The intensities and profiles of new peaks give a direct signature of molecular structure (distances between chromophores) and dynamics (the spectral density of the chromophores' environments). These techniques may be developed into a standard diagnostic tool to investigate hydrogen-bonded complexes, molecular liquids, the secondary and tertiary structure of polypeptides, protein folding, and chromophore aggregates. Multiple pulse techniques have the capacity to prepare electronic and vibrational degrees of freedom in nonequilibrium states and monitor their subsequent dynamics, yielding femtosecond snapshots of dynamical processes, vibrational and electronic energy transfer pathways, charge transfer, photoisomerization, and chemical reactions. The observation of cross peaks and the analysis of their magnitudes and line shapes provide extremely powerful microscopic probes of local environments. The various possible techniques may be systematically classified and described using Liouville space pathways (1), which represent the relevant sequences of population and coherence periods that dominate the multiple-pulse nonlinear optical response of complex molecules. Experiments performed on a single chromophore coupled to a bath probe purely nuclear response and solvation. The multimode Brownian oscillator model commonly used in the analysis of such measurements has been reviewed (14) and is not discussed. 2D vibrational Raman spectroscopy was first proposed by Loring & Mukamel (15) as an extension of coherent Raman 1D techniques. 2D vibrational Raman techniques have been reviewed recently (16) and are not considered here.

In this review we discuss the design and interpretation of nD measurements in systems of coupled localized electronic or vibrational chromophores. The fundamental theoretical concepts underlying these techniques and their systematic interpretation and the information content of various experimental configurations are classified and compared. A direct attempt to compute optical excitations in large molecules and aggregates seems like a hopeless task because computing the global eigenstates involves a complex many-body problem and requires a massive numerical effort. Moreover, even if such calculations could be carried out, they usually do not provide much physical insight because of the large number of interfering contributions. These difficulties can be overcome by making a radical change of view: Rather than following the dynamics of the actual particles (electrons and nuclei), we reformulate the problem in terms of new fictitious quasiparticles representing collective elementary excitations. The optical response is then

attributed to couplings, scattering, and dephasing of these quasiparticles. The quasiparticles are weakly interacting, and in practice in typical applications it is sufficient to consider only a few of them. We thus obtain a computationally affordable algorithm that lends itself easily to physical insight. The celebrated Lorentz model of the electron that describes the linear response using a Drude-oscillator is an example of a quasiparticle (1). A systematic extension of this model to nonlinear spectroscopy, which provides a rigorous quasiparticle picture, is given by the nonlinear exciton equations (NEE), which are described and applied in this review.

We consider a model that applies to two classes of systems: (*a*) electronic (visible) excitations in molecular aggregates (17) such as J aggregates (18, 19) or the photosynthetic reaction center (20) and antenna complexes (21–24); (*b*) vibrational (infrared) excitations of coupled, localized high-frequency modes, for example the amide I band in proteins and polypeptides that originates from the stretching motion of the $C{=}O$ bond (coupled to in-phase $N{-}H$ bending and $C{-}H$ stretching) (25–31), or hydrogen-bonded complexes and liquid water (32–39). 1D spectroscopy in both types of systems yields a few broadened features that depend on numerous factors, such as intermolecular couplings, exciton localization, disorder, and coupling to phonons. It is impossible to pinpoint these various factors unambiguously using the limited information provided by 1D lineshapes. Optical excitations of coupled chromophores can be separated into manifolds with different numbers of excitons (Figure 1*A*) (17, 40–42a). Femtosecond techniques can probe the entire manifolds of states in a single measurement and 2D plots then reveal the correlations between the various chromophores. A variety of ultrafast nonlinear spectroscopic techniques, such as pump probe, photon echo, and hole burning applied to molecular aggregates, provide direct signatures of the exciton structure and energy migration (43–49).

One of the pressing issues in the study of chromophore aggregates is whether the elementary optical excitations are localized on a few molecules or delocalized across the entire complex. The excitation coherence size is determined by the interplay of intermolecular couplings and (static as well as dynamic) disorder. We show that multidimensional techniques reveal a multitude of time-dependent coherence sizes associated with various dynamical variables, with specific spectroscopic signatures.

Multidimensional coherent spectroscopies are commonly used in multiple-pulse NMR to disentangle complex spectra of many interacting spins by spreading them along several time (or frequency) axes (11–13, 50–52b). The advent of femtosecond laser pulses has made it possible to apply similar concepts in the optical regime. Despite the similarity, the resulting information is different and complementary. In 2D NMR, radiowave pulses act on nuclear spins, the timescales are milliseconds or longer, and spin-spin correlation functions are being probed. Similarly, 2D electron spin resonance applies microwave pulses to electronic spins (53–53b). Multidimensional microwave techniques have also been used to study molecular rotations (54, 54a). Vibrational spectroscopy probes anharmonicities using either infrared or visible pulses (Raman) whereas electronic spectroscopy
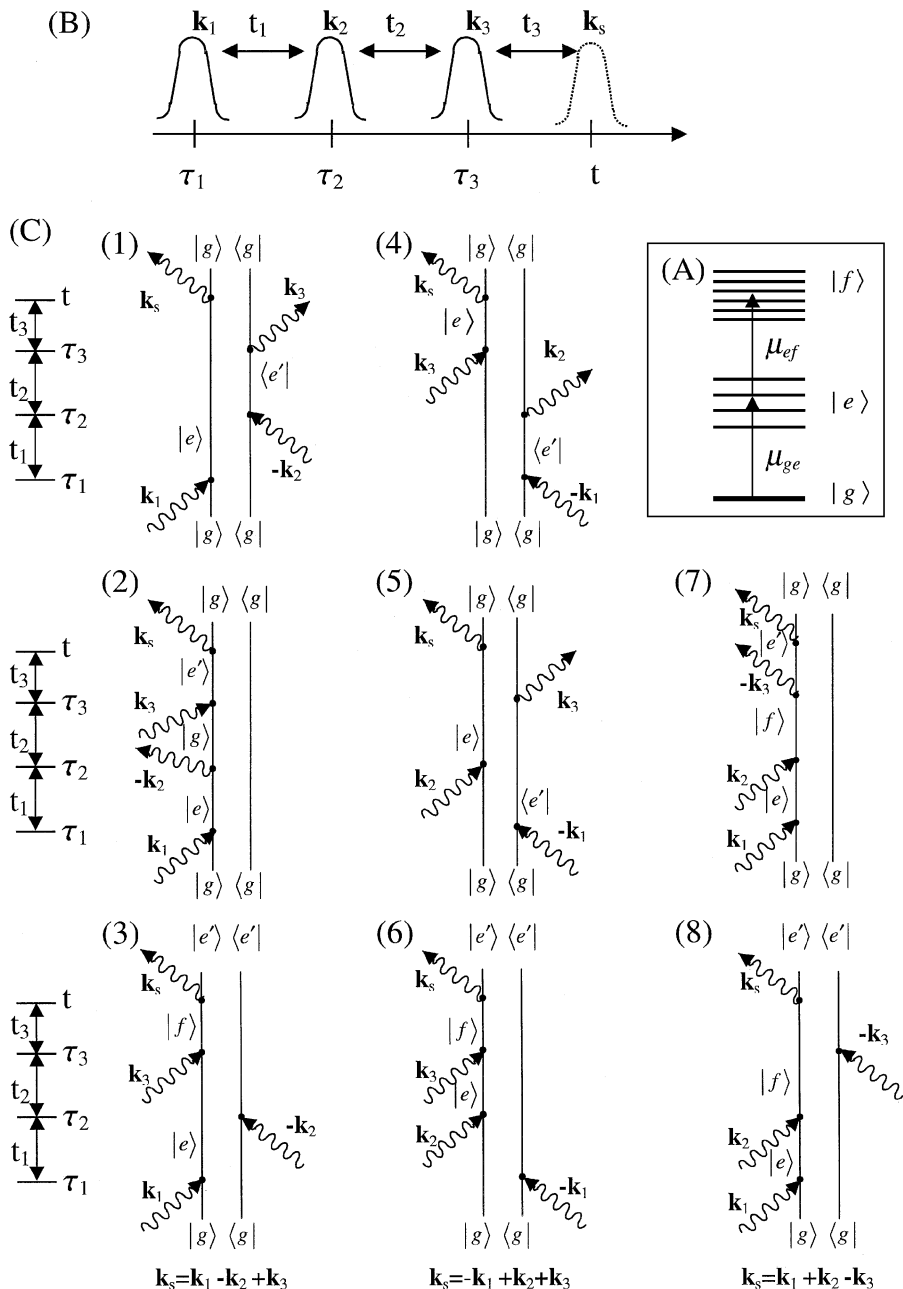
Figure 1 (A) Level scheme of a molecular aggregate. Shown is the ground state $|g\rangle$, the single-exciton $|e\rangle$, and the two-exciton $|f\rangle$ manifolds. (B) Pulse sequence in a three-pulse experiment. (C) Double-sided Feynman diagrams representing the Liouville space pathways contributing to the third-order response of A in the rotating wave approximation. Each *column* shows the diagrams contributing to a four-wave mixing signal in a distinct direction $\mathbf{k_s}$, as indicated. The rotating wave approximation does not permit a signal in the fourth possible wavevector $\mathbf{k}_s = \mathbf{k}_1 + \mathbf{k}_2 + \mathbf{k}_3$.

uses ultraviolet or visible pulses to probe electronic dynamics on the femtosecond timescale (2, 55–60a). These techniques could become potentially as powerful as nD NMR. NMR is too slow to resolve many interesting processes (61), and a structure determination based on optical pulses could push the time resolution from milliseconds all the way to femtoseconds. Dynamical events induced by optical pulses can be directly probed by X-ray pulses (diffraction, absorption, fluorescence) which provide femtosecond snapshots of molecular structure without the restrictions imposed by the dipole selection rules in optical probes (62–64). Comparison of multidimensional NMR with vibrational and electronic spectroscopies will undoubtedly stimulate new experiments and allow insights gained in one field to be adopted in another. The well-developed machinery of multidimensional NMR may be adapted to optical spectroscopy for probing specific vibrational and electronic motions and interactions. Multiple-pulse NMR sequences probing multiple-quantum coherences provide important structural tools because they are sensitive to geometry and coupling patterns. Infrared and visible techniques have the potential to become as valuable.

NONLINEAR RESPONSE FUNCTIONS AND MULTIDIMENSIONAL SIGNALS

Probing electronic and nuclear couplings and dynamics with multidimensional spectroscopy involves the application of n well-separated pulses that generate and manipulate populations and coherences of electronic and vibrational states. We assume that the jth pulse centered at τ_j has an envelope $\mathcal{E}_j(\tau - \tau_j)$, carrier frequency ω_j, and wavevector $\mathbf{k}_j$, and that the total field at point $\mathbf{r}$, $\mathcal{E}(\mathbf{r}, t)$ is given by

$$\mathcal{E}(\mathbf{r}, \tau) = \sum_{j=1}^{n}[\mathcal{E}_j(\tau - \tau_j)\exp(i\mathbf{k}_j\mathbf{r} - i\omega_j\tau) + \mathcal{E}_j^*(\tau - \tau_j)\exp(-i\mathbf{k}_j\mathbf{r} + i\omega_j\tau)].$$

1.

The induced polarization (and the signal field) is altogether nth order in the applied fields

$$P^{(n)}(\mathbf{r}, t) = \int_0^\infty dt_1 \ldots \int_0^\infty dt_n R^{(n)}(t_n, \ldots, t_1)$$
$$\times \mathcal{E}(\mathbf{r}, t - t_n) \ldots \mathcal{E}(\mathbf{r}, t - t_1 \ldots - t_n).$$

2.

Optical pulses are controlled by many parameters (5, 6, 65). In the following we assume that the pulses are very short (impulsive) compared with all relevant molecular timescales, allowing the independent control of the n time intervals $(t_1, t_2, \ldots t_n)$. For $n = 3$, the excitation pulses come at times $\tau_1 = t - t_1 - t_2 - t_3$, $\tau_2 = t - t_2 - t_3$, and $\tau_3 = t - t_3$, where t_1, t_2, are the delay times between the

pulses and t_3 is the delay time between the last excitation pulse and the actual time t when the signal is measured (see Figure 1B) (controlling the last t_n interval requires an additional gating device or heterodyne detection). The microscopic information carried by the signal is given by the response function $R^{(n)}$, which constitutes an n-dimensional (nD) spectroscopy. $R^{(n)}$ can in turn be expressed as combinations of $n + 1$ order correlation functions of the dipole operator (1)

$$R^{(1)}(t_1) = \left(\frac{i}{\hbar}\right) \langle [\mu(t_1), \mu(0)] \rangle;$$

$$\qquad\qquad 3.$$

$$R^{(2)}(t_2, t_1) = \left(\frac{i}{\hbar}\right)^2 \langle [\mu(t_2 + t_1), [\mu(t_1), \mu(0)]] \rangle;$$

and so forth. Here the time evolution of the dipole $\mu(t)$ is given by the free molecular Hamiltonian (in the absence of the driving fields). The computation and the interpretation of the response functions is the key in designing new techniques and extracting the desired information.

Computing a specific signal requires an examination of the dependence of the phase of $P^{(n)}$ on position n. When Equation 1 is substituted in Equation 2, we find that $P^{(n)}(\mathbf{r}, t)$ generally has several contributions, each depending on $\mathbf{r}$ through an $\exp(i\mathbf{k_s} \cdot \mathbf{r})$ factor where the wavevector $\mathbf{k_s}$ is one of the 2^n possible combinations $\mathbf{k}_s = \pm\mathbf{k}_1 \pm \mathbf{k}_2 \ldots \pm \mathbf{k}_n$. Each of these contributions, when substituted in Maxwell's equations, will generate a distinct signal field in the corresponding $\mathbf{k_s}$ direction. This is the case provided the sample is larger than the signal wavelength $\mathbf{k_s}^{-1}$, which is typically satisfied in optical measurements. In NMR, the reverse is true, and the signal lacks directionality. An equivalent information is obtained then by tuning the phases of the pulses. Phase-matching conditions connected with the frequency dispersion of the index of refraction may favor some of these wavevectors and discriminate against others. Each choice of $\mathbf{k_s}$ also implies a particular combination of field frequencies $\omega_s = \pm\omega_1 \pm \omega_2 \ldots \pm \omega_n$ (see Equation 1). Consequently, when a particular choice is made, only some of the contributions to $R^{(n)}$ will be resonant with the fields and make a significant contribution to $P^{(n)}$. The resonant signal is dominated by these contributions. All other terms are highly oscillatory and may be safely neglected. This is known as the rotating wave approximation (RWA). For three-pulse ($n = 3$) spectroscopies there are eight possible wavevectors for the signal. Only four of them are independent because $\mathbf{k}_s$ and $-\mathbf{k}_s$ represent essentially the same technique. It is possible to derive a universal expression for $R^{(n)}$ which applies for an arbitrary multilevel system (1). However, the choice of terms that survive the RWA and contribute to a given $\mathbf{k}_s$ depends on the specific molecular level scheme and the dipole couplings. For our model aggregate (Figure 1A), we find that only three wavevectors survive the RWA. The corresponding double-sided Feynman diagrams are shown in Figure 1C. [See chapter 6 of ref. (1) for the rules for these diagrams.]

The three columns show the 3, 3, and 2 diagrams contributing to $\mathbf{k}_s = \mathbf{k}_1 - \mathbf{k}_2 + \mathbf{k}_3$, $-\mathbf{k}_1 + \mathbf{k}_2 + \mathbf{k}_3$, and $\mathbf{k}_1 + \mathbf{k}_2 - \mathbf{k}_3$, as indicated. The contributions to the fourth possible wavevector $\mathbf{k}_1 + \mathbf{k}_2 + \mathbf{k}_3$ are negligible within the RWA. Note that

four diagrams run over one-exciton states $|e\rangle$ only, and the other four include the two-exciton $|f\rangle$ states as well.

Let us consider a specific choice of a wavevector $\mathbf{k_s}$ in a three-pulse impulsive experiment and denote the corresponding RWA response function by $\mathcal{R}_s(t_3, t_2, t_1)$. Various detection modes that probe different projections of the third-order response function $\mathcal{R}_s(t_3, t_2, t_1)$ may be employed (1, 2, 7–9, 66–70). The time-gated homodyne signal is given by $|\mathcal{R}_s(t_3, t_2, t_1)|^2$. Frequency-dispersed homodyne detection gives $|\mathcal{R}_s(\omega_3, t_2, t_1)|^2$, where

$$\mathcal{R}_s(\omega_3, t_2, t_1) = \int dt_3 \mathcal{R}_s(t_3, t_2, t_1) \exp(i\omega_3 t_3). \qquad 4.$$

The conventional homodyne signal is obtained by integrating the time-gated signal over t_3. These homodyne techniques probe $|P^{(n)}(t)|^2$. However, more elaborate detection schemes can detect $P^{(n)}(t)$ itself and thus give the complete electric field signal (both amplitude and phase). These techniques provide an additional useful design tool for nD spectroscopies because they yield both real and imaginary parts of $\mathcal{R}_s$, rather than merely $|\mathcal{R}_s|^2$. This can be achieved by mixing the signal with an additional phase-locked heterodyne pulse. Both time and frequency gating configurations have been employed. Other gated detection modes such as FROG (65) or SPIDER (71) are frequently used to detect the complete electric field. A convenient way to visualize the signal field is by displaying its Wigner spectrogram, which is bilinear in the response function (57, 57a, 69, 72)

$$S(\omega_3; t_3, t_2, t_1) = \int d\tau \mathcal{R}(t_3 + \tau/2, t_2, t_1) \mathcal{R}^*(t_3 - \tau/2, t_2, t_1) \exp(i\omega_3 \tau) \qquad 5.$$

and represents the time-dependent spectrum of the field. This provides a clear representation of the amplitude and phase of the signal. The time-gated (frequency-dispersed) signals are obtained by integrating the spectrogram over frequency (ω_3) or time (t_3). Each pair of dynamical variables of the signal S may be used to generate a distinct 2D correlation plot. An ω_3, t_3 plot, for example, shows the Wigner spectrogram of the signal field.

QUASIPARTICLE (REAL-SPACE) VERSUS EIGENSTATE (ENERGY-SPACE) PICTURES OF OPTICAL RESPONSE

We consider an aggregate made of N interacting three-level molecules with transition frequencies Ω_m and Ω'_m, where $m = 1 \ldots N$, and transition dipoles μ_m and μ'_m, respectively (see Figure 2). We assume that these are the only nonvanishing matrix elements of the dipole operator. The global states of the aggregate are displayed in Figure 1A. This exciton model represents assemblies of molecules with nonoverlapping charge distributions such as molecular crystals (40, 41), photosynthetic complexes (73, 74), supramolecular structures (75, 76), organic superlattices (77), dendrimers (78–80a), J aggregates (18), and localized vibrations (25, 26, 29, 30, 30a).
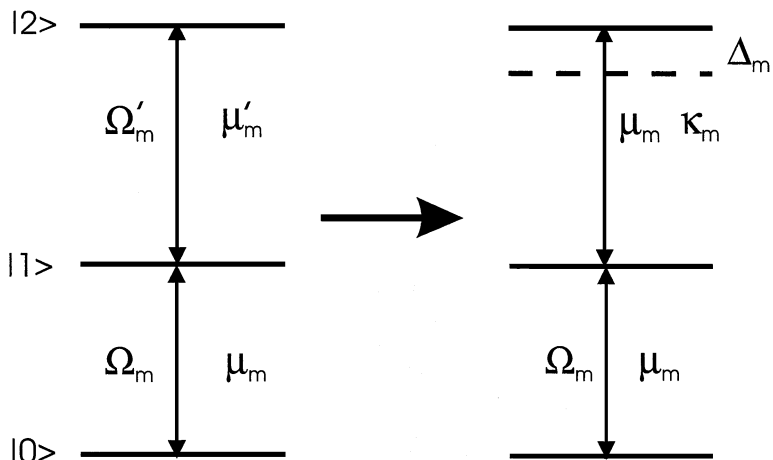
Figure 2 Mapping of the three-level system (*left*) onto the excitonic-oscillator (quasiparticle) model (*right*). $\Delta_m = \Omega'_m - \Omega_m$ is the anharmonicity parameter. κ_m represents the ratio of the two transition dipoles.

The optical response functions may be computed by expanding them in the molecular eigenstates. The complete set of double-sided Feynman diagrams representing the Liouville-space pathways contributing to the third-order response function of our model aggregate in the RWA are given in Figure 1*C*. The linear optical (1D) response usually probes one-exciton states alone, whereas third-order 2D and 3D techniques involve two-exciton states as well. As the degree of nonlinearity is increased, successively higher manifolds become accessible. Third order techniques are useful because the pattern of multiple excitations provides an extremely sensitive probe for aggregate structure and connectivity of the various chromophores.

It is possible to describe the aggregate as a supermolecule and compute the response functions using sums over its global eigenstates, as depicted in Figure 1*C* (81–83). These expressions have several limitations. First, they rapidly become more complex as the aggregate size increases [because there are N one-exciton states, $N(N + 1)/2$ two-exciton states, and numerous matrix elements of the dipole]. Experimental polarizabilities, on the other hand, attain a simple limiting value for large sizes. Second, they contain very large terms, typically one group $\sim N^2$ and another $\sim N(N - 1)$, which almost cancel, resulting in an overall $\sim N$ scaling (84, 85). These arguments suggest that something is ill posed in the eigenstate representation. It may be used for small systems with sparse, well-resolved levels. However, it is impractical to describe the dynamics of large aggregates using their global eigenstates. These states are hard to calculate and carry much more information than is provided by spectroscopic measurements: A description in terms of the global states that follows the complete dynamics of electrons and nuclei is neither feasible nor desirable.

For these reasons it makes sense to switch to a completely new language that follows the excitations directly (rather than the global eigenstates). The resulting *quasiparticle* approach provides an alternative classical anharmonic oscillator picture of the optical excitations (42, 42a). To develop this collective approach, we associate with each molecule an anharmonic oscillator degree of freedom [in some cases it is desirable to assign several oscillators to each molecule (86)] with fundamental frequency Ω_m and creation (annihilation) operators $B_m^\dagger$ (B_m). We further introduce the following parameters: $\kappa_m \equiv \mu_m'/\mu_m$ denotes the ratio of the two transition dipoles, and $\Delta_m = \Omega_m' - \Omega_m$ is the anharmonicity. The original model of interacting three-level molecules with parameters $(\Omega_m, \Omega_m', \mu_m, \mu_m')$ can thus be mapped into coupled anharmonic oscillators characterized by the parameters Ω_m, Δ_m, μ_m, and κ_m (Figure 2). The single-exciton manifold is described by the Hamiltonian $H = \sum_{mn} h_{mn} B_m^\dagger B_n$, where $h_{mn} = \delta_{mn} \hbar \Omega_m + J_{mn}$, and the couplings J_{mn} among chromophores are small compared with Ω_m. The coupling with the radiation field $\mathcal{E}(t)$ is given by $-\mathcal{E}(t) P$, where $P = \sum_n \mu_n (B_n + B_n^\dagger)$ is the polarization (dipole) operator.

The nonlinear exciton equations (NEE) provide a powerful quasiparticle framework for the computation and analysis of the nonlinear response and nD spectroscopies of excitons (42, 42a). These equations that establish a collective oscillator picture for exciton dynamics underlying the nonlinear response have been gradually developed over the past few years (84–89). To introduce the quasiparticle picture, we start with the Heisenberg equation of motion for B_m (90),

$$i \frac{d}{dt} \langle B_m \rangle = \sum_n h_{mn} \langle B_n \rangle - \frac{\mu_m}{\hbar} E_m(t) + \left[\Delta_m - \left(\kappa_m^2 - 2 \right) \Omega_m \right] \langle B_m^+ B_m B_m \rangle$$

$$+ \left(\kappa_m^2 - 2 \right) \sum_n h_{mn} \langle B_m^\dagger B_m B_n \rangle - \left(\kappa_m^2 - 2 \right) \frac{\mu_m}{\hbar} E_m(t) \langle B_m^\dagger B_m \rangle. \quad 6.$$

Here $\langle \ldots \rangle$ denotes a quantum mechanical expectation value. We first note that if the energy levels of the molecule form a harmonic ladder, then $\Delta_n = 0$, $\kappa_n = \sqrt{2}$, the last three terms in the right-hand side vanish, and Equation 6 becomes *linear*. Consequently, the induced polarization will always be linear in the applied field, and all nonlinear response functions $R^{(2)}$, $R^{(3)}$, etc, must vanish identically. This is the celebrated Lorentz oscillator model for the linear response (1). In the global states picture, the vanishing of the nonlinear response is a result of a delicate interference among many Liouville-space pathways. Only when all the terms are carefully added do they exactly cancel, reflecting a destructive interference of various nonlinear paths. In contrast, in the equation of motion this interference is naturally built in from the start, avoiding the computation of spurious almost-canceling quantities.

Except for the harmonic case, Equation 6 is not closed because $\langle B_m \rangle$ is coupled to higher dynamical variables. The NEE supplement Equation 6 by equations for the additional multi-exciton variables $\langle B_m \rangle$, $\langle B_m B_n \rangle$, $\langle B_m^+ B_n \rangle$, and $\langle B_j^+ B_m B_n \rangle$, representing single-exciton dynamics, two-exciton dynamics, the exciton density

matrix, and a three-point exciton-coherence, respectively (42, 42a). These constitute the complete set of dynamical variables required for the microscopic description of all spectroscopies that depend on the optical field up to third order. Higher variables including, for example, four B_n factors only enter in higher order in the field. This can be rationalized as follows. The Frenkel-exciton Hamiltonian conserves the number of excitations. Nonconserving processes are controlled by the ratio of intermolecular coupling to the optical frequency, which is typically small. This simplifies the problem considerably because the spectrum consists of well-separated groups of energy levels representing single excitations, double excitations, etc, as shown in Figure 1A. Because only the radiation field can change the number of excitations, we can classify optical techniques according to their power dependence on the incoming fields, and very few types of electronic excitations need to be considered at each order. This provides a convenient computational strategy as well as the basis for an intuitive physical picture. The infinite manybody hierarchy of dynamical variables is thus rigorously truncated order by order in the radiation field, allowing an exact calculation of the nonlinear response functions for this model. $\langle B_m B_n \rangle$ is responsible for two-exciton resonances, whereas $\langle B_m^+ B_n \rangle$ is the exciton density matrix responsible, for example, for fluorescence, pump-probe, and transient grating spectroscopies. In the notation of Equation 5, the dynamics of $\langle B_n \rangle$ is dominant during the t_1 and t_3 periods whereas $\langle B_n^+ B_m \rangle$ and $\langle B_n B_m \rangle$ represent the evolution during t_2. Nuclear variables are traced out and incorporated through relaxation superoperators calculated to second order in exciton-phonon coupling.

The solution of the NEE yields expressions for the optical response in terms of Green functions representing the free dynamics of the various variables when the external field is switched off. For example, for the single-exciton variables, we have

$$\langle B_m(t) \rangle = \sum_n G_{mn}(t) \langle B_n(0) \rangle. \qquad 7.$$

Similarly we introduce a Green function for the $\langle B_m B_n \rangle$ variables that describes the motion of two excitons and exciton-exciton scattering, and a third Green function for the exciton density matrix $\langle B_n^+ B_m \rangle$ that describes incoherent exciton motion induced by exciton-phonon scattering. The response is represented in terms of these three Green functions (42, 42a).

The NEE provide a collective nonlinear oscillator picture for exciton dynamics and the nonlinear response. Optical nonlinearities are generated by the deviations from the linearly driven harmonic model, which enter through anharmonicities, nonlinearities in the expansion of the polarization operator in powers of the primary variables, and the non-boson nature of the primary variables (deviations from boson statistics). These induce exciton scattering processes, which in turn give rise to optical nonlinearities.

Expressing the optical response through scattering of quasiparticles (rather than the more traditional picture of transitions among global eigenstates) immediately

cures the earlier-discussed problems associated with the global eigenstate picture and provides an extremely useful physical insight with greatly reduced computational effort. Moreover, by describing the optical response in real space, it provides a most natural and intuitive picture, which is particularly suitable for the interpretation of femtosecond spectroscopies. The solution of the NEE in real space assumes the form (58, 91–91b)

$$R^{(1)}(t_1) = \sum_{n,m} (\mu_n \cdot \hat{e}_2)(\mu_m \cdot \hat{e}_1) R_{nm}(t_1), \qquad 8.$$

$$R^{(3)}(t_3, t_2, t_1) = \sum_{n,m_1,m_2,m_3} (\mu_n \cdot \hat{e}_4)\left(\mu_{m_3} \cdot \hat{e}_3\right)\left(\mu_{m_2} \cdot \hat{e}_2\right)\left(\mu_{m_1} \cdot \hat{e}_1\right)$$
$$\times R_{n,m_1,m_2,m_3}(t_3, t_2, t_1). \qquad 9.$$

$R^{(n)}$ is an $n + 1$ rank tensor whose components represent the possible polarization directions of the various fields. In Equation 9, $\hat{e}_1, \hat{e}_2, \hat{e}_3$ are unit vectors denoting the polarization directions of the incoming fields, and the signal field is polarized along $\hat{e}_4$. Equation 9 naturally breaks the signal into two factors. The product of four μs is a *geometric* factor that depends on the orientations of the various transition dipoles, whereas $R_{nm_1m_2m_3}$ represents exciton-dynamics; the polarization created at a site n, due to fields interacting at the m_1, m_2, and m_3 sites.

The merits of the quasiparticle approach may be rationalized by the following dichotomy: The traditional expansion of the response in delocalized exciton eigenstates makes sense because the time evolution may be conveniently represented by these states. However, the expression for the dipole operator that is the window through which the dynamics is observed is much simpler in real space because it is a sum over contributions of individual molecules. Consequently, the real-space picture provides a transparent and computationally superior scheme for complex systems.

The utility of the NEE equations has been demonstrated by a successful modeling of numerous nD measurements in photosynthetic antenna complexes (73–73b). These include absorption, fluorescence depolarization and time-resolved Stokes shift, cooperative spontaneous emission (superradiance), hole burning, and pump probe.

LIOUVILLE-SPACE PATHWAYS AND CROSS PEAKS FOR COUPLED CHROMOPHORES

To demonstrate how multidimensional spectroscopy works and how it may be used to extract information about structure and coupling patterns of interacting chromophores, we present 2D signals computed using third-order ($R^{(3)}$) techniques (Figure 1) where two out of the three pulses (denoted **k** and **k′**) coincide in time. Four such techniques that satisfy the RWA are possible (Figure 3): (*a*) photon echo (PE) $\mathbf{k}_s = \mathbf{k}_2' + \mathbf{k}_2 - \mathbf{k}_1$, where $\mathbf{k}_1$ refers to the first pulse and $\mathbf{k}_2'$ and $\mathbf{k}_2$ represent

(A)
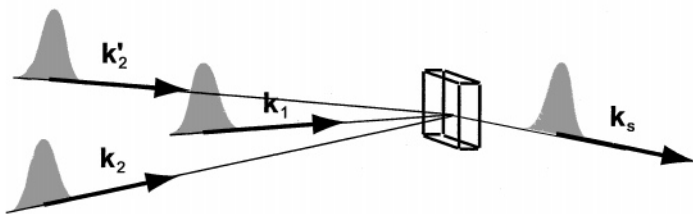
(B)
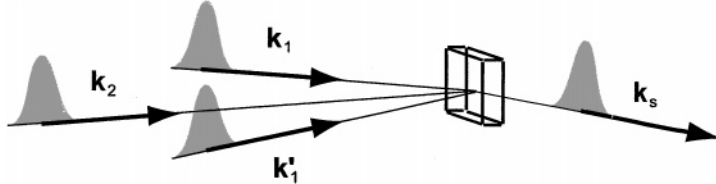
Figure 3   Pulse sequences for two-dimensional three-pulse techniques. (*A*) The single pulse comes first, followed by the pulse pair $\mathbf{k}_s = \mathbf{k}'_2 + \mathbf{k}_2 - \mathbf{k}_1$ (photon echo), and $\mathbf{k}_s = -\mathbf{k}'_2 + \mathbf{k}_2 + \mathbf{k}_1$ (reverse transient grating). (*B*) The pulse pair comes first, followed by the single pulse $\mathbf{k}_s = -\mathbf{k}_2 + \mathbf{k}'_1 + \mathbf{k}_1$ (reverse photon echo), and $\mathbf{k}_s = \mathbf{k}_2 - \mathbf{k}'_1 + \mathbf{k}_1$ (transient grating).

the second and third pulses; (*b*) the reverse PE (RPE) $\mathbf{k}_s = -\mathbf{k}_2 + \mathbf{k}'_1 + \mathbf{k}_1$, where the pulse-time ordering is reversed; (*c*) transient grating (TG) $\mathbf{k}_s = \mathbf{k}_2 - \mathbf{k}'_1 + \mathbf{k}_1$; and (*d*) reverse TG (RTG) $\mathbf{k}_s = -\mathbf{k}'_2 + \mathbf{k}_2 - \mathbf{k}_1$. These techniques are special cases of the diagrams of Figure 1: The PE is given by the *middle column* with $t_2 = 0$; the RPE is represented by the *right column* with $t_1 = 0$; the TG is given by the *left* and the *middle columns* with $t_1 = 0$; and the RTG is given by the *left* and the *right columns* with $t_2 = 0$.

The heterodyne signal can be displayed and analyzed either in the time or in the frequency domain by defining the Fourier transform $S(\Omega_2, \Omega_1)$ of the time-domain signal $\hat{S}(T_2, T_1)$ with respect to the two relevant time delays (42, 42a, 56, 56a):

$$S(\Omega_2, \Omega_1) = \int_0^\infty dt_1 \int_0^\infty dt_2 e^{i\Omega_1 T_1 + i\Omega_2 T_2} \hat{S}(T_2, T_1). \qquad 10.$$

Despite its frequency-domain appearance, Equation 10 represents a time-domain technique that is merely displayed in Ω-space because it maintains a

complete control over time ordering.[1] Ω_1 and Ω_2 are associated with the first and the second time intervals, respectively, and thus carry different types of information. This is markedly different from frequency-domain measurements described by optical susceptibilities that are invariant to permutations of field frequencies (1).

Intermolecular interactions can be directly probed by examining the cross peaks in the double Fourier transforms of the response functions. Useful structural information can thus be derived from the intensities of cross peaks between localized chromophores.[2] To illustrate this, we consider a system of three two-level chromophores labeled A, B, and C, with transition frequencies Ω_A, Ω_B, and Ω_C. Calculations were made for the following two models: In the first the chromophores are totally decoupled $J_{mn} = 0$, whereas in the second the chromophores are coupled. Both models were constructed to have precisely the same absorption spectrum shown in Figure 4a. Obviously, the linear absorption alone does not reveal the couplings among chromophores. The 2D spectra are, however, completely different. The sensitivities of all four techniques to intermolecular couplings J is illustrated in the model calculations shown in Figure 4. In the *left column*, we display $|S(\Omega_2, \Omega_1)|$ for the first (no-coupling) model. Only diagonal peaks at the individual chromophore frequencies show up. We introduce the notation (Ω_i, Ω_j) to identify the abcissa (Ω_i) and ordinate (Ω_j) of peaks in the 2D plot. The PE shown in Figure 4c has diagonal peaks at $(-\Omega_A, \Omega_A)$, $(-\Omega_B, \Omega_B)$, $(-\Omega_C, \Omega_C)$. In Figure 4e (TG), the peaks are at $(0, \Omega_A)$, $(0, \Omega_B)$, and $(0, \Omega_C)$ whereas for the RTG (Figure 4g) the peaks are at (Ω_A, Ω_A), (Ω_B, Ω_B), and (Ω_C, Ω_C). RPE is not shown because the signal vanishes for this model, reflecting the absence of doubly excited states on single chromophores (86). In the *right column*, we display the 2D spectra for the second model, where coupling between chromophores has been included. Figure 4b gives the RPE. Starting from the second row, we display the 2D spectrum for each technique next to its decoupled model spectrum in the *left column*. Figure 4d shows the PE. Apart from the diagonal peaks shown in Figure 4c, we observe additional off-diagonal cross peaks, such as $(-\Omega_A, \Omega_B)$ $(-\Omega_A, \Omega_C)$, etc. As the coupling strength is increased, additional cross peaks appear at combinations of frequencies e.g. $(-\Omega_A, \Omega_B + \Omega_C - \Omega_A)$ (not shown). Figure 4f and h, which represent the TG and RTG techniques, show cross peaks as well. These simulations illustrate how 2D (in contrast to 1D) spectroscopies carry detailed information on intermolecular coupling constants. 2D spectra can

---

[1]Note that T_1 and T_2 in Equation 10 can be either t_1, t_2, or t_3 in the notation of Equation 2, depending on the specific technique. For the PE and RTG techniques, we set $T_1 = t_1$, $t_2 = 0$, $T_2 = t_3$, and $\hat{S}(T_2, T_1)$ is related to $R^{(3)}(T_2, 0, T_1)$. For RPE and TG, we set $t_1 = 0$, $T_1 = t_2$, $T_2 = t_3$, and $\hat{S}(T_2, T_1)$ is related to $R^{(3)}(T_2, T_1, 0)$.

[2]A word of caution: Heterodyne phase-controled detection probes the field $P(t)$ whereas homodyne detection measures $|P(t)|^2$. Cross terms thus appear in the homodyne signal even when they are absent in P itself. This effect generated by interference between macroscopic electric fields yields no additional microscopic information, even though it may provide a convenient detection mode (88).
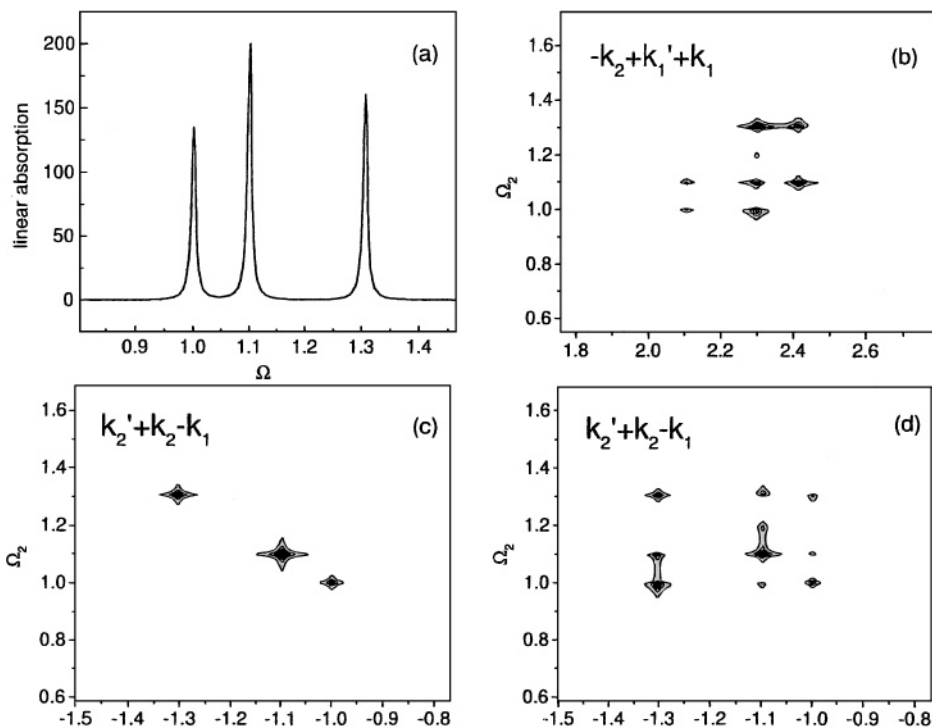
Figure 4 (*Left column*) Two-dimensional signals for three uncoupled chromophores A, B, C with optical frequencies (in dimensionless units) 1.366, 1.501, 1.783. (*Right column*) Signals for three coupled chromophores. These two systems have exactly the same linear absorption (*a*). (*b*) Reverse photon echo; (*c* and *d*) photon echo; (*e* and *f*) transient grating; (*g* and *h*) reverse transient grating. Distinct signatures of intermolecular couplings are clearly seen by comparing the *right* and *left columns* (42a).

distinguish between different coupling patterns even when the linear absorption is identical.

Each of these techniques gives a distinct cross-peak pattern that carries different types of information on intermolecular couplings and molecular structure. The intensities of the off-diagonal peaks carry information on the magnitudes of intermolecular couplings, whereas the peak widths represent dephasing processes. For $J = 0$, the signal $S(\Omega_2, \Omega_1)$ is given by the sum of contributions from individual chromophores and is, therefore, represented by a set of diagonal peaks located at the diagonal $\Omega_2 = \Omega_1$. To first-order in J, the signals show a series of new off-diagonal cross peaks whose Ω_1, Ω_2 coordinates give the transition frequencies of different chromophores. The intensities of these peaks provide the complete information on intermolecular coupling constants. To second order in J, new cross peaks at combinations of the chromophore frequencies appear as
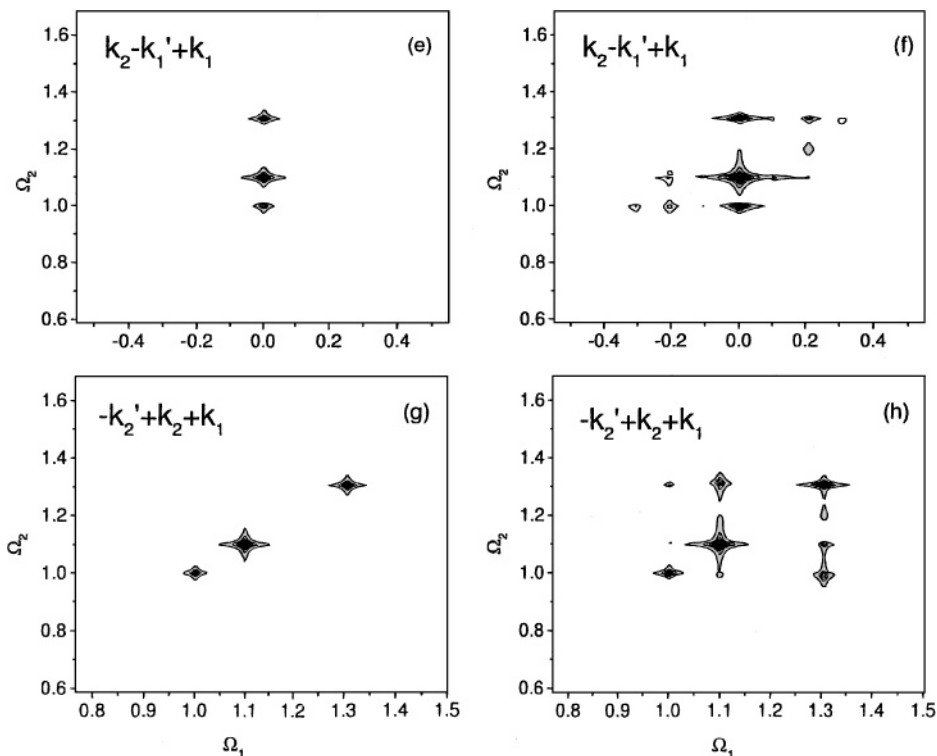
Figure 4   (*Continued*)

well. The couplings J may be directly obtained from the off-diagonal peak intensities. For strong intermolecular coupling when J is of the order of the differences between the chromophore transition frequencies, the peak positions are shifted because of excitonic effects. The information on J may then be extracted from both peak positions and intensities.

The application of electronically resonant 2D and 3D spectroscopies toward refining the structure of photosynthetic antenna complexes is an appealing possibility. For example, the FMO (Fenna-Matthew-Olson) complex is made out of three monomers each having seven chlorophyll A chromophores. A structure that includes the dipole orientations was proposed (92–92b). Although only minor differences were found in the positions and orientations of the various BCHls in the two species studied, their low-temperature optical spectra show significant differences. This indicates that the local environment and site energies in the two complexes differ considerably. Another important application is to the LHCII complex, whose structure and composition is under debate. Kuhlbrandt et al (93) proposed a structure with 7BChl a and 5 BChl b. However, the identification of these two types of chlorophylls and their orientation in the X-ray structure is controversial,

since ordinary optical methods do not provide a unique structure (93–95). A simpler and better-characterized model system for LHCII is the CP29 complex which consists of 6 Chl a and 2 Chl b molecules (96). The chlorosomes (96) are giant cylinderically shaped aggregates of Chl B which are much less characterized. 2D spectroscopies should be ideal for resolving existing discrepancies and providing fine details of structure and couplings in these aggregates.

REAL-SPACE REPRESENTATION OF EXCITONIC-RESPONSE AND COHERENCE-SIZES

Exciton Eigenstates Versus Density Matrices

One of the most frequently asked questions in the photophysics and photochemistry of aggregates is whether the chromophores act independently or cooperatively. It is widely accepted that there should exist some sort of a coherence size that represents the effective number of chromophores acting collectively. The most popular and obvious measure is the exciton localization size. Consider the eigenstates of the single-exciton Hamiltonian $|\Psi_\alpha> = \sum_n \Psi_\alpha(n)|n>$, with $\Psi_\alpha(n)$ being the normalized wavefunction for the αth exciton. A convenient measure of the effective number of chromophores contributing to a given exciton state is the inverse participation ratio (97)

$$L_\alpha = \frac{1}{\sum_n |\Psi_\alpha(n)|^4}. \qquad 11.$$

For a localized exciton, $L_\alpha = 1$; for delocalized exciton, $\Psi_\alpha(n) = 1/\sqrt{N}$ and $L_\alpha = N$. Generally, L_α interpolates between these two extremes. However, L_α is usually not directly and simply related to specific dynamical observables. Physical properties are given by wavepackets of exciton states and require averaging over many exciton eigenstates. Since different measurements prepare different wavepackets, an excitonic system will generally have a multitude of coherence sizes, which can be detected by nD spectroscopies. L_α fails to reflect this diversity. In addition, coupling with other degrees of freedom, whether slow (static-disorder) or fast (phonons), requires ensemble averagings. Such averagings should be performed over the signal; an ensemble-averaged exciton wavefunction is meaningless.

The exciton density matrix $\rho_{mn} = \langle B_m^+ B_n \rangle$ provides a natural real-space measure of exciton localization. When the exciton eigenstates are well resolved and the experiment depends on a few of them, it is possible to interpret the optical response using properties of individual eigenstates. However, in many cases, these properties are averaged out by the collective nature of the measurement. This happens, for example, at finite temperatures (compared with the exciton bandwidth). In addition, when exciton-phonon coupling is incorporated, the pure exciton states are not very meaningful because we need to consider the eigenstates in the joint

electronic and nuclear spaces. Computing these eigenstates is expensive and not very insightful. The exciton density matrix provides a level of description most compatible with optical measurements and is therefore the natural link between theory and experiment.

A convenient measure for delocalization of the exciton density matrix is provided by the inverse participation ratio L_ρ, defined by (73–73b)

$$L_\rho(t) \equiv \frac{\left(\sum_{nm} |\rho_{mn}(t)|\right)^2}{N \sum_{mn} |\rho_{mn}(t)|^2}, \qquad 12.$$

where N is the number of chromophores. This quantity gives the length scale on which the density matrix decays along the antidiagonal direction, i.e. as a function of $n - m$. Similar measures have been used in the analysis of off-resonant polarizabilities of aggregates (85, 87), conjugated polymers (98–98b), and semiconductor nanocrystals (99). The density-matrix coherence size (Equation 12) provides precisely the level of averaging required for the description of many optical signals and dynamical processes.

The issue of the coherence size has a conceptual significance as well as important practical implications to theoretical modeling. If, in practice, coherence sizes are small, a description in terms of delocalized exciton states though formally correct is misleading. A local (real space) description should be much simpler and more natural. The exciton states often carry a false and unphysical coherence that eventually cancels once physical properties are calculated. A real-space density matrix description (e.g. Equation 9) should allow us to perform a calculation on a small segment of the system and never worry about the long-range coherence, greatly reducing numerical effort.

The following calculations illustrate the influence of temperature and disorder on the density-matrix ρ_{nm} (73–73b). Calculations were made for the B850 band of the peripheral antenna of purple bacteria (LH2), a circular aggregate made out of 18 BCla chromophores. The thermally equilibrated reduced-density matrix assumes the form $\rho_{mn} \sim \sum_\alpha \Psi_\alpha^*(m) \Psi_\alpha(n) \exp(-\epsilon_\alpha/k_B T)$, where T is the temperature.

Figure 5a–c shows the anti-diagonal sections of the density matrices ρ_{mn} calculated for different temperatures and disorder strengths. Neglecting disorder and assuming a temperature lower than the splitting between the lowest excitons, only the lowest exciton is populated in thermal equilibrium. The corresponding density matrix will be delocalized over the entire ring, and $L_\rho = 18$ is equal to the systems' physical size. With increasing temperature, higher exciton states are populated, and ρ becomes more localized. This effect is illustrated in Figure 5a, where the canonical density matrices for temperatures 50 K (*solid*), 100 K (*dashed*), and 300 K (*dotted*) are displayed. Temperature-induced loss of coherence can be clearly seen with the corresponding values of L_ρ, which are 14.6, 10.5, and 5.95, respectively. In the high-temperature limit, all exciton states are equally populated and the density matrix becomes completely localized (diagonal in real space),

Figure 5 Localization of thermally relaxed exciton density matrices of LH2. (*a*) Purely exciton systems (no disorder and phonons), for different temperatures 50–300 K. (*b*) For different disorder strengths at temperature 4 K (73a).
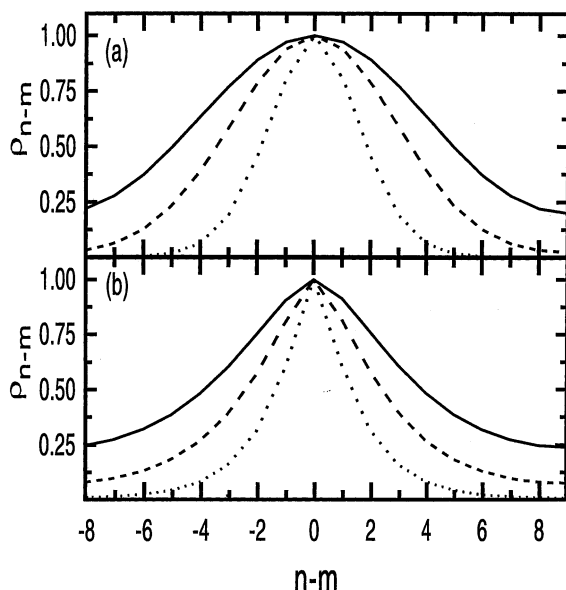
resulting in $L_\rho = 1$ even when all individual exciton states are delocalized. At higher temperatures, higher-energy excitons with oscillatory wavefunctions are populated, thereby decreasing L_ρ. Under these conditions, L_ρ is primarily determined by phase cancellation and not by exciton localization.

Figure 5*b* illustrates how disorder leads to localization of the density matrix at low temperatures. Energetic diagonal disorder has been included by assuming that the Ω_n have independent Gaussian distributions with the same mean frequency $\bar{\Omega}$ (independent of n) and full width at half maximum σ. Calculations were made using a Monte-Carlo sampling over different realizations. As shown in Figure 5*b*, this localization becomes stronger with increasing σ. The corresponding values of L_ρ at 4 K are 14.6, 10.6, and 6.16 for $\sigma = 330\,\text{cm}^{-1}$, $565\,\text{cm}^{-1}$, and $1130\,\text{cm}^{-1}$, respectively. In the limit of very strong disorder, the density matrix becomes completely localized (diagonal) and we have $L_\rho = 1$. The localization of ρ can also be induced by polaron formation due to strong coupling with phonons (not shown).

These calculations illustrate the major differences between the coherence sizes associated with the density matrix (L_ρ) (Equation 12) and individual eigenstates (L_α) (Equation 11). If the eigenstates are localized, then the density matrix must be localized as well. The reverse is not true: The density matrix may be localized even if the individual states are delocalized. At low temperature, only low-energy excitons with nonoscillatory wavefunctions are populated, and L_ρ is related to the exciton localization length L_α. Even when L_ρ is determined by localization, its numerical value does not coincide with L_α. The relations between the two quantities depends on L_α, the wavefunction shape, and the system size. For various typical models, the ratio of L_α to L_ρ was found to vary between 1.0 to 3.3. Realistic simulations for LH2 gave $L_\rho \approx 3L_\alpha$ ($L_\rho = 15$ and $L_\alpha = 5$).

In the applications described in the remainder of this section, we discuss the coherence sizes underlying various 1D and 2D measurements. Rather than the static, energy-space measure based on the exciton eigenstates, we consider two dynamic real-space types of definitions of coherence size. First, for linear absorption we adopt a definition based on the nonlocal response functions (Equation 8). This measure, which uses two-time quantities, may be directly extended to nD techniques by using Equation 9. The peak splitting in pump-probe spectroscopy of photosynthetic antennae may be described by this measure as well. Second, the coherence size underlying cooperative spontaneous emission and sequential pump-probe and gated fluorescence measurements that probe exciton migration is connected with L_ρ. The first measure uses a two-time correlation function of the free molecule whereas the second is based on a single-time expectation value of the optically driven system.

Linear Absorption

We start with the coherence size associated with linear absorption. The absorption lineshape of polarized light is given by

$$\alpha(\omega) = \sum_{nm} \text{Im}[(\mu_n \cdot \hat{e})(\mu_m \cdot \hat{e})G_{nm}(\omega)], \qquad 13.$$

where the exciton Green function is given by

$$G_{nm}(\omega) = \sum_\alpha \frac{\Psi_\alpha(n)\Psi_\alpha^*(m)}{\omega - \omega_\alpha + i\Gamma_\alpha}, \qquad 14.$$

$\hat{e}$ is the unit vector determining the direction of light polarization, and Γ_α is the dephasing rate of the $\alpha's$ exciton state with energy ω_α. It could represent lifetime (radiative or not) or pure dephasing. The origin of Γ_α makes no difference in the following analysis. By averaging over all possible orientations of $\hat{e}$, the linear absorption of depolarized light is given by Equation 13, with $(\mu_n \cdot \hat{e})(\mu_m \cdot \hat{e})$ replaced by $(\mu_n \cdot \mu_m)$. The one-exciton Green function may be alternatively recast in the form

$$G_{mn}(\omega) = \int_0^\infty d\tau \, \exp(i\omega\tau)\langle B_m(\tau)B_n^\dagger(0)\rangle, \qquad 15.$$

where $B_m(\tau)$ is the time-dependent operator for the free aggregate (without the field).

According to Equation 13, the linear absorption is directly related to the exciton coherence size at energy ω, $L_f(\omega)$. This coherence size is defined as the inverse participation ratio associated with the exciton Green function (73), and is given by Equation 13, with ρ_{mn} replaced by $G_{mn}(\omega)$. L_f is the length scale on which the exciton Green function decays along the antidiagonal direction, i.e. as function of $n - m$.

For narrow homogeneous width $\Gamma_\alpha \ll |\omega_\alpha - \omega_{\alpha'}|$, the exciton lines are well resolved and the optical excitation selects a single exciton state $\omega = \omega_\alpha$. In this

case, $G_{nm}(\omega) \approx \frac{1}{\Gamma_\alpha} \Psi_\alpha(n) \Psi_\alpha^*(m)$. Because the exciton wavefunctions contain a $\sim 1/\sqrt{N}$ normalization factor, the Green function scales as $G_{nm}(\omega) \sim 1/N$ and $L_f = N$ representing complete delocalization of the excitation over all chromophores. In the opposite limit of a very large width, the exciton lines overlap strongly, simplifying the expression for the Green function $G_{nm}(\omega) \approx \frac{1}{\Gamma} \sum_\alpha \Psi_\alpha(n) \Psi_\alpha^*(m) = \frac{1}{\Gamma} \delta_{nm}$. Now the Green function scales with N as $G_{nm}(\omega) \sim 1$, and $L_f = 1$ representing complete localization of the electronic excitation on a single chromophore. For intermediate values of Γ, $L_f(\omega)$ varies between 1 and N, providing a convenient measure of the relevant exciton size at frequency ω.

It is possible to define the coherence size for linear absorption using an alternative, kinematic view based on exciton wavepackets and their mean free path. The radiation field with frequency ω excites several exciton states lying within the bandwidth Γ, creating a wavepacket with momentum spread Δk. Because the exciton energy depends on its momentum $\omega(k)$, one finds that $\Gamma \sim \Delta\omega = (\partial\omega(k)/\partial k)\Delta k$. According to this, the exciton coherence size is

$$L_f \equiv \frac{2\pi}{\Delta k} = \frac{2\pi}{\Gamma} \frac{\partial\omega(k)}{\partial k}. \qquad 16.$$

This is simply the exciton mean free path defined as the product of the exciton wavepacket group velocity $u = \partial\omega(k)/\partial k$ and its lifetime $\tau = 2\pi/\Gamma$. The dispersion relation of 1D excitons in the vicinity of the exciton band edge ($k \sim 0$) is $\omega = 2JN^2k^2$. This gives the exciton coherence size $L_s = 4JN^2k/\Gamma$. Both descriptions lead to identical results but provide different types of physical pictures. The kinematic approach is more traditional and is commonly used for molecular crystals. The real-space picture uses a local (molecular) basis whose size is small and is most natural for excitons in complex disordered aggregates.

This analysis may be extended to techniques that make use of the tensor character of the linear response [e.g. circular dichroism spectroscopy (100, 100a)] and can be used to identify different types of coherence sizes. Our definition based on linear response (the distance between typical n, m in Equation 13) can further be extended to the nonlinear response functions. We can define s as the center of mass of m_1, m_2, m_3 in Equation 9 and examine the dependence of the contributions on the distance between s and n. We can also look at any of the time intervals, e.g. for the first interval we focus on m_1, m_2 and we can further look at the distance of s to m_1, s to m_2, etc. All of these definitions use various two-time quantities to show the characteristic distance between two prescribed events.

Peak Splitting in Pump-Probe Spectroscopy

Pump-probe spectroscopy provides a direct view into excitonic motions through the differential absorption of a probe pulse as a function of its frequency and time delay with respect to a pump pulse. Technically this is a $P^{(3)}$ self heterodyne technique whereby the probe serves as the heterodyne field. The frequency-

dependent differential absorption typically contains a negative peak related to bleaching and to stimulated emission from the one-exciton band to the ground state (we refer to both contributions as BL), and a positive peak that reflects excited state absorption (ESA) from one-exciton to two-exciton states (84, 101, 102). The pump-probe signal can be interpreted using a three-level model that contains the ground state and the lowest one-exciton and two-exciton states. The spectral shift $\Delta\Omega$ between these two features is then attributed to the energy difference between the exciton state prepared by the pump and a two-exciton state coupled radiatively to that exciton by the probe. In a linear aggregate made out of N molecules, we have $\Delta\Omega \approx 3\pi^2 J/(N+1)^2$, where J is the nearest neighbor exciton intermolecular interaction (in circular aggregates $\Delta\Omega = 4\pi^2 J/N^2$). The shift in the pump-probe signal of J aggregates has been observed by Wiersma's group and fitted using a model of a linear aggregate of physical size $N = 15$ with nearest neighbor interaction $J = 1227$ cm^{-1} derived from the frequency shift between the aggregate and the monomer absorption peaks. This coherence size was attributed to the exciton localization length induced by static disorder (103, 103a). Similar observations have been made in both LH1 and LH2 antenna complexes (101, 102), where the observed ~200 cm^{-1} shift in LH2 was reproduced by assuming that only a fraction of the monomers ($N = 4$) are coherently coupled.

Figure 6 shows the calculated pump-probe spectra of LH2 for different homogeneous widths Γ at 4.2 K (73–73b). For all values of Γ, the pump-probe signals show a negative BL part at lower energies and a positive ESA part at higher energies. For small Γ, the splitting $\Delta\Omega$ is small, indicating that this system has two-exciton states energetically very close to twice the one-exciton energy. The ESA shows a progression of several well-resolved two-exciton contributions. When the exciton dephasing Γ becomes larger than the splitting between exciton levels, the two-exciton resonance merge, and $\Delta\Omega$ increases (see Figure 6, *inset*). In this regime the shift reflects collective properties of the two-exciton manifold rather than positions of individual two-exciton states; the shift no longer reflects an energetic difference between specific states but is induced by, and scales with, the homogeneous line width. Under these circumstances, the pump-probe signal may not be interpreted in terms of a three-level model. Instead, the relevant coherence size then becomes the mean free path L_f introduced in the previous subsection.

Simulations of the pump-probe signal, incorporating both exciton-phonon interactions and static disorder (73–73b), reproduced the shift between the BL and ESA as well as their relative magnitude, in agreement with experimental pump-probe spectra on B850 of LH2 at 4.2 K (101, 102). These calculations show that the shift $\Delta\Omega$ between the positive and negative peaks is determined by the mean free path $L_f = 11$. A related coherence size is observed in saturated absorption measurements (104, 105), which are essentially a single-color pump-probe spectroscopy (the probe has the same frequency of the pump). The variation of the bleaching with pump intensity depends on the coherence size.
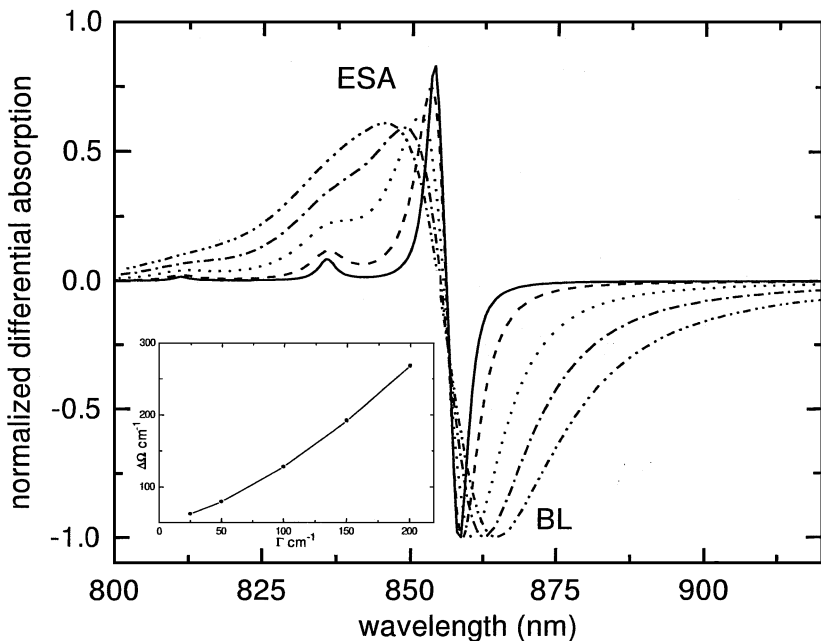
Figure 6 Normalized pump-probe spectra of the LH2 antenna without disorder for different dephasing rates Γ at 4.2 K. $\kappa = 0.9$. $\Gamma = $ (*solid*) 25 cm^{-1}, (*dash*) 50 cm^{-1}, (*dot*) 100 cm^{-1}, (*dash-dot*) 150 cm^{-1}, and (*dash-dot-dot*) 200 cm^{-1}. (*Inset*) Peak splitting $\Delta\Omega$ as a function of Γ. For other parameters see text. ESA, Excited state absorption (73).

Cooperative Spontaneous Emission: Superradiance

Time-resolved fluorescence may show cooperative spontaneous emission (superradiance), which is one of the most interesting elementary signatures of exciton localization and intermolecular coherence (106–108). This effect has a simple classical interpretation: When a collection of dipoles oscillates in phase, their amplitudes add up coherently to form a large effective dipole. The oscillator strength, and consequently the radiative decay rate, is then proportional to the number of dipoles. The superradiance coherence size L_s of a molecular aggregate is defined as the ratio of its radiative decay rate to that of a single molecule. (For simplicity we assume that all molecules are identical and have the same radiative decay rate.) Molecules separated by more than an optical wavelength λ may not emit coherently. $(\lambda/a)^d$ is therefore the ultimate electrodynamic upper bound for L_s, a being the lattice constant and d is the aggregate dimensionality. In practice, however, the coherence size is usually determined by other dephasing mechanisms, such as exciton-phonon interactions and static disorder, and is typically much smaller than both the aggregate physical size and the optical wavelength.

Superradiance has been reported in semiconductor quantum wells (109), J-aggregates (18, 19, 84), quantum wires (110), and σ-conjugated polysilaens (111). In J-aggregates of pseudoisocyanine dyes, a superradiance coherence size $L_s = 50$, which is much smaller than the number of molecules in the aggregate 5×10^4, has been reported. Coherence sizes of 2–3 were found in mixtures of isocyanine dyes absorbed on silver halide substrates at room temperature (112, 112a), whereas $L_s = 70$ has been reported for pseudoisocyanine aggregates in a low-temperature glass (106–106c,113, 113a).

L_s can be expressed in terms of the exciton density matrix, normalized to a unit trace, i.e. $\sum_n \rho_{nn} = 1$.

$$L_s(t) = \sum_{mn} (\mathbf{d}_m \cdot \mathbf{d}_n) \rho_{mn}(t), \qquad\qquad 17.$$

where $\mathbf{d}_m$ is a unit vector in the direction of the mth chromophore transition dipole. L_s is controlled by both the coherence-size L_ρ (Equation 12), associated with the antidiagonal section of the exciton density matrix ρ_{mn}, and the geometry (relative orientation of transition dipoles) through the $\mathbf{d}_m \cdot \mathbf{d}_n$ factors. If the molecular dipoles are parallel, the coherence size L_ρ characterizes the size of a domain where the molecules emit coherently, and L_s is then related to the number of molecules in this domain. Loss of coherence, which leads to the decrease of L_ρ, reduces L_s as well. In the opposite situation where the total dipole of an aggregate (i.e. the vector sum of the molecular dipoles) vanishes because of cancellation of contributions from individual molecules, the emission is induced by the loss of coherence, and L_s should increase with the decrease of L_ρ. Recent experiments on photosynthetic antenna complexes showed coherence sizes of 2–3 at room temperature, whereas at low temperatures $L_s = 3$ for LH2 antenna complexes and $L_s = 9$ for LH1. L_s was found to be virtually temperature independent between 4 K and 200 K (114). Simulations using the exciton density matrix reproduced these observations (73–73b).

An excellent correlation between L_s and L_ρ was found for several mechanisms of loss of coherence (finite temperature and disorder-induced dephasing) and orientations of the dipoles in LH2. This demonstrates that the localization of the density matrix, as viewed by its antidiagonal spread sections, controls the superradiance emission. L_s may thus be predicted from L_ρ, regardless of the specific microscopic mechanism that determines L_ρ.

Studies of single molecules in the condensed phase is an exciting new development made feasible through the combination of various forms of optical microscopy with ultrasensitive detection (115, 116). Ordinary bulk measurements provide highly averaged information. By eliminating ensemble averaging, SMS gives invaluable additional information regarding intramolecular dynamics and coupling with the surrounding. Spectroscopy of single antenna complexes (117–120) could yield the entire distributions (rather than merely the average value) of the various coherence sizes such as L_ρ or L_s. This could help distinguish between different models (e.g. weak vs. strong disorder) which may predict the same

average but a very different distribution (115) of coherence size. SMS distributions of fluorescence lifetimes and photobleaching properties of single LH2 complexes have been measured under physiological conditions (119). Low-temperature (1.2 K) single-molecule fluorescence excitation spectra of these complexes have been reported as well (120). Photobleaching kinetics shows how many chromophores a single trap can quench and thus provides a different type of coherence size. The statistics of the on/off bleaching periods depends on how the aggregate is dissected into effective chromophores (121). The photobleaching of one BChl molecule causes the total shutdown of fluorescence because of exciton trapping, which suggests complete delocalization (120). A correlation between the Stokes shift and superradiance in disordered aggregates may be another measure of time coherence size (122).

Exciton Migration in Fluorescence, Pump Probe, and Three-Pulse Techniques

Exciton transport and relaxation in chromophore aggregates shows signatures of complex physical phenomena: exciton-exciton scattering due to their repulsive (on site, Pauli exclusion) and attractive (e.g. dipole-dipole) interactions, elastic scattering and exciton localization due to static disorder, and inelastic exciton scattering and self-trapping induced by strong exciton-phonon coupling. Exciton migration can be probed by a variety of nonlinear spectroscopic techniques, such as pump probe, three-pulse echo, and the time- and frequency-gated fluorescence, and shows direct signatures of the exciton coherence size (48, 60, 60a, 73, 73b, 123, 124). For these techniques it may be possible to express the response in terms of a time-dependent exciton wavepacket represented by its density matrix. The spatial extent of this wavepacket constitutes the underlying relevant coherence size. To that end we recast the time- and frequency-resolved fluorescence using the doorway-window representation (1, 125).

$$S_{fl}(\tau, \omega) = \sum_{mnkl} \int_0^\infty d\tau' \int_0^\infty dt_2 \mathcal{W}_{nm}(\tau - \tau', \omega) G_{mn,kl}(t_2) \rho_{kl}(\tau' - t_2). \quad 18.$$

The doorway-window picture in Liouville space, first developed for describing the nuclear density matrix for vibrations and the solvent (126), offers an intuitive physical description of the sequence of events. In this picture, the signal's generation is described as a three-step process involving the preparation, propagation, and detection of a wavepacket representing the exciton density matrix. First, two interactions with the pump create the reduced exciton density matrix ρ_{mn} (the doorway wavepacket). The diagonal elements ($m = n$) of $\rho_{mn}(\tau)$ represent exciton populations whereas the off-diagonal elements ($n \neq m$) are excited state coherences. In the second step, the doorway evolves during the time delay between the pump and the detection stage. The Green function

$$G_{mn,kl}(t_2) \equiv \langle B_l(0) B_n^\dagger(t_2) B_m(t_2) B_k^\dagger(0) \rangle \quad 19.$$

describes the propagation of the doorway wavepacket and relaxation of excitons during the delay period t_2. In the NEE, this Green function is calculated by solving the Redfield equations, which describe the time evolution of the exciton density matrix $\rho_{nm}(t) \equiv \langle B_n^\dagger(t)B_m(t)\rangle$ (127–130). In the third step, the window wavepacket $\mathcal{W}$ is created by the spontaneously emitted photon together with the gating device, and the signal is finally computed as the overlap of the doorway and the window wavepackets in Liouville space.

The calculation of $S_{fl}(\tau;\omega)$ is simplified considerably when the exciton population-relaxation timescale is long compared with the inverse absorption line width (dephasing timescale), and the pump and gate are fast compared with the relaxation time but slow compared with the dephasing time. These conditions define the snapshot limit (1, 126) where the signal only depends on the pump and the gate frequencies and their relative delay and is independent on their precise envelopes. The doorway-window representation applies also to pump probe and to measurements performed with three well-separated pulses. This will simply involve different expressions for the doorway and the window. Similarly, depolarization measurements can be described by using polarization-dependent doorway and window.

Equation 18 allows us to analyze separately the roles of the pump (which determines the doorway) and the probe (which affects the window), and to distinguish between the roles of exciton dynamics and the system's geometry. The optical pulses and gating device may be described using Wigner spectrograms, utilizing a joint temporal and spectral representation of nonlinear spectroscopy (57, 57a, 69, 72). Wigner spectrograms account for arbitrary pulse shapes and durations and interpolate naturally between the impulsive (time-resolved) and the ideal frequency-resolved limits.

So far we have discussed exciton transport and dynamics using the NEE that apply when nuclear relaxation is much faster than exciton transport. In this case it is possible to follow the dynamics of the exciton density matrix $\rho_{mn}(t)$, where all vibrational degrees of freedom have been traced out.[3] The coupling to nuclei is incorporated via relaxation superoperators calculated perturbatively in exciton-phonon coupling. Such theory does not take the detailed form of nuclear spectral densities into account. The pump-probe signal, the frequency resolved fluorescence, and the superradiance in LH2 have been analyzed using this approach. Strong exciton-phonon coupling can be treated under certain conditions by keeping explicitly only the populations, resulting in the master equation. Master equations depend on the choice of the exciton basis set. When nuclear dynamics is not fast, one needs to use a higher level of theory that supplements the excitonic variables with a set of relevant collective vibrational variables that need to be treated

---

[3]Note that we are considering here a nonstationary density matrix representing the molecule driven by the pump field. The localization size can be alternatively obtained using the equilibrium correlation function $\langle B_m(0)B_n^\dagger(t)B_n(t)B_m^\dagger(0)\rangle$. Here the time evolution of all operators is given by the molecular Hamiltonian (without the external field). The localization length may then be visualized by examining the variation of this quantity with $n-m$ for long times).

explicitly as well, and that represent an arbitrary spectral density of a phonon bath. Such coupling may lead to the formation of polarons (excitons dressed by a phonon cloud). Coherent three-pulse techniques such as photon echo require this level of theory (57, 57a). A useful way of displaying multidimensional information in the photon echo technique (126a) is provided by 1D plots of the peak shift (59, 124, 131).

VIBRATIONAL ECHOES: PROBES OF STRUCTURE AND SOLVATION DYNAMICS

Vibrational motions provide an important window into the structure and dynamics of complex molecules, liquids, and proteins. Sequences of infrared pulses have been widely used to conduct vibrational echo measurements (31, 132–134a). Equilibrium fluctuations of a protein (myoglobin) and its slow conformational motion were studied by vibrational echo and pump-probe response of CO attached to the heme porphyrin (135–136c). Three pulse infrared photon echoes have been employed in studying solvent and protein fluctuations (135). The complex and disordered network of vibrations in hydrogen-bonded liquids such as water and alcohols have been extensively investigated using infrared pump probe and hole burning (32–34, 37, 137), and optical Kerr techniques (39). Optical spectroscopy of solvated chromophores in liquids and glasses provides a different multidimensional view of their local environment (35, 38, 38a, 138). Multiple resonance frequency-domain 2D infrared measurements have shown their capacity to disentangle congested vibrational spectra of solutes in various solvents (139–139c). This doubly vibrationally enhanced (DOVE) four-wave mixing technique probes the frequency-domain third-order susceptibility $\chi^{(3)}$ rather than the response function $R^{(3)}$. 2D analysis of 1D infrared spectra has proven useful in identifying cross correlations among vibrational features (140). Vibrational relaxation of polyatomic molecules usually proceeds via well defined pathways, which could be identified by multidimensional measurements.

Earlier, (Equation 6) we showed that all higher nonlinearities $P^{(2)}$, $P^{(3)}$, etc, vanish identically for harmonic vibrations whose dipole depends linearly on nuclear coordinates (1, 85). Higher-order optical vibrational response can be induced by various sources of nonlinearity, such as nonlinear dependence of the dipole μ on nuclear coordinates, anharmonic intermolecular and intramolecular potentials that contain terms cubic and higher in the coordinates, and relaxation and dephasing by nonlinear coupling to a bath (16, 141). The various types of nonlinearities affect the response in a different way and may thus be extracted from experimental signals (16, 30, 30a, 42, 42a). The nonlinear dipole creates intermode coherences instantaneously each time the system interacts with the radiation field. In contrast, the effect of anharmonicity is not felt immediately because such a coherence may only be built during the evolution period between such interactions. The resonance structure and phase of 2D signals contain distinct 2D signatures of both types of nonlinearities. If the various vibrational modes do not interact (e.g. when

they represent different components of inhomogeneous regions), the nonlinearities will be diagonal, and the contributions of the various modes to the nonlinear response will be additive. Off-diagonal couplings will however result in cross terms.

Below we present simulations of 2D vibrational echoes in polypeptides (30), which demonstrate their capacity to view molecular structure and probe dynamical events such as protein folding (142–143). We focus on the 1600–1700 cm^{-1} amide I band, which has a strong transition dipole moment and is clearly distinguishable from other vibrational modes of the amino acid side chains (144). The dependence of its frequency on a particular secondary structure is widely utilized in polypeptide and protein structure determination (25–27). This band consists of a number of poorly-resolved spectral lines associated with vibrational motions of different structural elements. Conformational fluctuations within a particular 3D structure and local interaction with water induce inhomogeneous broadening, and the spectrum is highly congested. Protein folding into a complex 3D structure, which consists of several polypeptide segments forming different types of secondary structures, results in strong interactions between remote CO bonds, which strongly affect the structure of exciton states (26).

The transition dipole coupling tensor between the CO stretching modes results in the delocalization of vibrational states (25) and in splittings of individual spectral lines. The dependence of this tensor on relative orientation and distances of the interacting dipoles results in a unique amide I band, characteristic of the particular 3D conformation (25).

Dipole-dipole coupling leads to coherent energy transfer between the stretching modes and the formation of delocalized vibronic excitations (vibrons), analogous to Frenkel excitons. Strong coupling to slow vibrational motions may lead to exciton localization and self-trapping, which could be probed by multidimensional spectroscopic signals. Good agreement with experiment has been obtained in the modeling of this band for a few mid-size globular proteins with known structures (26). Resolution-enhanced infrared techniques such as Fourier transform infrared spectroscopy have been employed in the determination of the protein secondary structure (145). However, such 1D methods only provide a limited information.

The structure of the one-exciton and two-exciton manifold of the pentapeptide [cyclo(Abu-Arg-Gly-Asp-Mamb)] (Figure 7) has been probed using 2D infrared techniques. The simplicity of the cross-peak structure for this pentapeptide, and the presence of β-turn, makes it ideal for testing 2D techniques and establishing the signatures of anharmonicity and diagonal vs off-diagonal disorder in 2D spectra. Incoherent femtosecond experiments such as pump probe and hole burning as well as coherent photon echoes have been carried out on this system and other polypeptides (28, 29, 31). The atomic coordinates of this pentapeptide are known from its crystallographic structure measurements and NMR, shown in Figure 9 (see color insert). The backbone conformation of each polypeptide traces out a rectangular shape with a β-turn centered at the Abu-Arg bond. In the simulations presented below (30), we model each CO bond as a three-level system (Figure 2). The dipole-dipole couplings among CO vibrations were

calculated using the known geometry. The cyclic structure of the compound allows vibrational energy migration along the ring, which could be studied by applying the TG (RTG) techniques (Figure 3). Using the real-space basis, the two-exciton manifold, which consists of $N(N + 1)/2$ states, can be divided into two submanifolds. One is formed by N states, representing vibrational dynamics of doubly excited peptides (overtones). The other $N(N - 1)/2$ states represent simultaneously excited single vibrational states of different peptide groups. The PE (RPE) techniques (Figure 3) can distinguish between contributions of these manifolds, sort out diagonal and off-diagonal disorder couplings, and determine the signatures of localized exciton dynamics (30, 30a).

Static disorder due to variations in local protein structure induces inhomogeneous spectral broadening and exciton localization. Study of disorder effects, energy transport along secondary structure motifs, and exciton state correlations should reveal the dynamics of excitons localized on different secondary structure elements, its dependence on the local structures, and its manifestation in 2D infrared spectra. Three models of inhomogeneous line broadening have been employed in the following calculations: no inhomogeneous broadening (Figure 8*A*), uncorrelated static diagonal disorder (distribution of the vibrational frequencies) (Figure 8*C*), uncorrelated static off-diagonal disorder affecting the coupling tensor, due to various conformations (Figure 8*E*). These models included a small homogeneous broadening. When a larger and more realistic homogenous broadening is added to these models, we obtain the models shown in Figure 8*B*, *D*, *F* respectively. The linear (1D) absorption spectra of all models are presented in Figure 8. Figure 8*A* shows five well-resolved one-exciton lines. The resolution is reduced in the other panels. Because off-diagonal disorder induces exciton delocalization, the one-exciton resonances shown in Figure 8*E* and *F* are shifted compared with the other panels.

Figure 9 (see color insert) compares the absolute value of the 2D PE signal $|S(\Omega_2, \Omega_1)|$ for models *A*–*F* calculated using the NEE approach. Because the photon echo eliminates inhomogeneous broadening, all resonances in Figure 9 have the homogeneous width, e.g. along Ω_2 for Ω_1 fixed. The resonances representing various correlations between one-exciton states $(-\varepsilon_a, \varepsilon_a)$ (diagonal peaks) and $(-\varepsilon_a, \varepsilon_b)$ $a \neq b$ and $a, b = 1, \ldots, 5$ (off-diagonal peaks), as well as between one- and two-exciton states $(-\varepsilon_a, \bar{\varepsilon}_b - \varepsilon_a)$, $a, b = 1, \ldots, 5$ (cross peaks), are well resolved in Figure 9*A*, *C*, and *E*, which have a very small homogeneous broadening. Figure 9*B*, *D*, and *F* have the same resonant energies; however, because homogeneous broadening is comparable with the anharmonicity and coupling energies, many resonances are unresolved. Figure 9*C*–*F* shows inhomogeneously broadened resonances stretched along the $-\Omega_1 = \Omega_2$ direction. In Figure 9*C* and *D*, the excitons are localized, and energy differences between the maxima of one-exciton and strong two-exciton resonances are equal to the anharmonicity Δ. The excitons in panels 9*E* and *F* are delocalized.

These simulations demonstrate how *n*D spectroscopies can be effectively used to probe the structure of disordered aggregates. In the absence of intermolecular
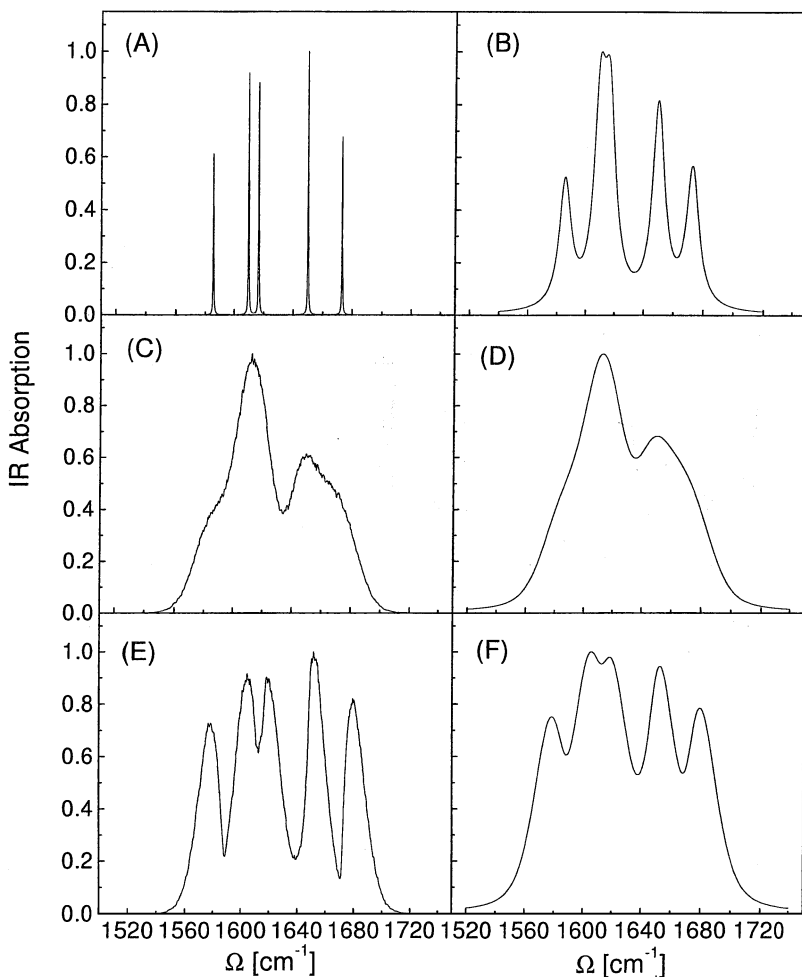
Figure 8 Infrared (IR) absorption (one dimensional) spectra for models (*A–F*) (30).

couplings, each realization of disorder gives a set of diagonal peaks. Averaging over realizations yields a signal whose magnitude along the diagonal direction reflects the total broadening (homogeneous and inhomogeneous) whereas its variation in the off-diagonal direction is related to the homogeneous component alone. Increasing intermolecular couplings leads to new off-diagonal peaks. Selective excitation with phase-locked pulse sequences, varying phase shifts between the pulses, and applying other 2D and 3D techniques and pulse sequences (42) should allow resolution of close homogeneously broadened 2D resonances, which are poorly resolved in Figure 9. The heterodyne-detected real and imaginary parts of the PE signal carry additional information. This is illustrated in Figure 10*B,D*,

and F (see color insert). Analysis of the sign variation of the real and imaginary parts in different directions (30, 30a) indicates that for close disorder realizations, the resonances should add up constructively in the directions $-\Omega_1 \sim \Omega_2$, and destructively in the perpendicular direction.

2D spectroscopies should provide an ideal tool for real-time observation of early folding events in proteins and polypeptides. The determination of protein structure and its relation to biological activity constitutes an important fundamental problem. Protein folding from a random coil into their native structure and the formation of α-helices or β-sheets is a complex process that extends over a broad range of timescales from femtoseconds to minutes (141–143). The nanosecond-to-millisecond formation of protein secondary and supersecondary structures are early events in this sequence. Because time resolution of NMR measurements is limited to milliseconds, they cannot be used to probe the early folding events (61). Conformational changes in proteins and polypeptides on nanosecond and longer timescales have been observed using laser-induced temperature jump (T-jump) (146, 147) transient infrared absorption (136–136c, 148–150) and fluorescent probe technique (151). One-dimensional infrared absorption techniques only provide highly averaged information regarding the empirically assigned secondary structure motifs whereas fluorescence provides local information on a specific segment interacting with the probe. Monitoring of fine details in secondary structure formation predicted by kinetic models (151) is not possible by these techniques. 2D infrared spectroscopies should provide a unique tool for studies of structural changes and protein folding with subpicosecond time resolution. Exciton dynamics is sensitive to the geometry of protein fragments where the exciton is confined and should provide a local probe of secondary structure and dynamics of hydrogen bonding. No other technique has this unique combination of spatial and temporal resolution.

FUTURE OUTLOOK

In this review we surveyed a new family of coherent nonlinear spectroscopic techniques made possible by recent advances in femtosecond laser technology, which provide new windows into the structure of molecular aggregates, the relevant coherence sizes, and the dynamics of complex structure-function relationships in molecules. A description of the optical response in terms of interacting quasiparticles provides a convenient framework for computing and interpreting the resulting multidimensional signals. Applications of multidimensional techniques toward probing the structure of proteins and photosynthetic aggregates and determining the interactions of chromophores with the local protein and solvent environment were described. Multidimensional signals carry specific signatures of coherent and incoherent energy and charge transfer, vibrational relaxation, and intramolecular and intermolecular dynamics on many timescales. High temporal resolution of dynamical processes such as chemical reactions, protein folding, and equilibrium

fluctuations of solvents is made possible. nD infrared techniques may be effectively used to study neat hydrogen-bonded liquids and solvated chromophores.

Some highly successful experimental methods have been established for the elucidation of molecular structure. In particular, X-ray crystallography, neutron diffraction, and nuclear magnetic resonance (NMR) spectroscopy provide accurate "images" of molecules. Intramolecular motion is only indirectly contained in the elucidated structures. For studying the molecular motion experimentally, NMR is at present the most versatile and powerful tool. Fast motional processes in the picosecond to microsecond range can be sampled indirectly by NMR relaxation experiments.

Nonlinear optical spectroscopy has been developed to a stage at which it can become complementary to NMR methods. Different optical and IR techniques are also capable to cover the whole range of timescales occurring in protein dynamics. Yet the information obtained from these measurements is much more direct than the results obtained from NMR relaxation experiments since optical techniques can follow the dynamics in real-time. The assumptions and approximations necessary to invert optical data and to obtain dynamical models for proteins are fundamentally different from those invoked in NMR. Therefore optical experiments provide an independent view on molecular dynamics that can be used to validate the NMR results, or to gain insight into processes that cannot be studied by NMR due to experimental limitations.

Significant progress has been made in this rapidly developing field, which is still in its infancy, and considerable joint experimental and theoretical effort will be required in order to develop it into a routine structural and dynamical diagnostic tool. On the experimental side, new pulse sequences should be explored. Heterodyne techniques that are common in the radiowave region and have been extended for visible pulses need to be developed in the infrared. Multidimensional vibrational spectroscopy can also be conducted using Raman techniques (16, 152), which have a better time resolution than infrared and can therefore excite vibrations impulsively. These are more complicated techniques because they are higher (for example, 2D spectroscopy is third order in the infrared but fifth order for Raman). In addition, technical problems of phase matching and interference with sequential lower-order processes (cascading) need to be overcome (153–155).

The complex nature of vibrational and electronic motions compared with spins requires new computational algorithms for analyzing these spectroscopies and connecting them with the underlying microscopic motions. The fundamental differences and similarities between multidimensional NMR and optical techniques should be taken into account. Spins are elementary quantum systems whose Hamiltonian depends on a few universal parameters. The theoretical analysis of anharmonic vibrations and electronic excitations is considerably more complex and requires the development of new concepts and tools. Automated inversion algorithms that could yield the inter-chromophore couplings and ultimately the structure directly from the signals without human intervention have yet to be developed.

Combining optical with NMR techniques for structure determination is an interesting and promising future development.

Extracting structural and dynamical information from experimental signals involves the computation of nonlinear response functions, taking into account anharmonicities, nonlinear dependence of the dipole on nuclear coordinates, and the quantum character of nuclear motions. $R^{(n)}$ is given by a sum of 2^n, $(n+1)$–order correlation functions, each representing a distinct Liouville space pathway for the system's density matrix (1). Nonlinear response functions (156, 157, 157a) show interesting classical interferences and depend on the stability matrix, which relates the changes in coordinates and momenta at two different times along a classical trajectory (16). This matrix, which carries the necessary information related to the vicinity of the trajectory, plays an important role in the studies of classical chaos. For each initial phase-space point, we need to launch n trajectories with very close initial conditions in order to compute $R^{(n)}$. The nonlinear response is obtained by adding the contributions of these trajectories and letting them interfere. These delicate interference effects, which pose serious computational difficulties, have the potential of directly probing the Lyapunov exponents that characterize chaotic systems.

Methods for classical and quantum simulations of two-point correlation functions are well established (37, 158). The development of efficient sampling and simulation algorithms for multiple-time correlation functions (156, 157, 157a, 159, 160) should be primary goals of future studies. Two practical semiclassical simulation strategies, one is a conventional high-temperature approximation and the other applies for weak anharmonicity regardless of temperature, have been proposed (161). An alternative strategy is to use analytically solvable models (e.g. multilevels with fluctuating parameters such as transition dipoles and frequencies) and compute the necessary correlation functions from these simulations. Reduced equations of motion for relevant collective coordinates may be used to that end. The relevant statistical properties of unresolved low-frequency intermolecular modes could be incorporated through 2D spectral densities (58).

The exciton model requires a prior knowledge of the nature of optical excitations. The many-body electronic problem is simplified considerably because the chromophores are well separated in space, their interactions are purely Coulombic (electron-exchange is negligible), and each chromophore retains its own electrons. Combining the modeling with quantum chemistry codes such as time-dependent density functional theory (163–165) should allow full account of exchange interchromophore couplings and a microscopic modeling of charge separation among chromophores (166–170). For example, three-pulse coherent techniques provide direct signatures of electron correlations in conjugated molecules (162, 162a) and semiconductors (171). Real-space quantum chemistry approaches (98, 98b) that directly relate optical properties of very large molecules to charge distributions in excited states and motions of electrons and holes in real space should provide a sound microscopic basis for simulations that will connect various femtosecond spectroscopies with the relevant underlying electronic and vibrational coherence sizes.

ACKNOWLEDGMENTS

Visit the Annual Reviews home page at www.AnnualReviews.org

LITERATURE CITED

1. Mukamel S. 1995. *Principles of Nonlinear Optical Spectroscopy.* New York: Oxford Univ. Press

2. Elsaesser T, Fujimoto JG, Wiersma DA, Zinth W, eds. 1998. *Ultrafast Phenomena XI.* Berlin: Springer-Verlag

3. Weiner AM, Leird DE, Weiderrecht GP, Nelson KA. 1990. *Science.* 247:1317

4. Tull JX, Dugan MA, Warren WS. 1997. *Advances in Magnetic and Optical Resonances.* 20:1

4a. Tull JX, Dugan MA, Warren WS. 1997. *J. Opt. Soc. Am. B* B14:2348

5. Steinmeyer G, Sutter DH, Gallmann L, Matuschek N, Keller U. 1999. *Science* 286:1507

6. Brabec T, Krausz F. 1997. *Phys. Rev. Lett.* 78:3282

7. Pshenichnikov MS, Duppen K, Wiersma DA. 1995. *Phys. Rev. Lett.* 74:674

7a. Emde MF, deBoeij WP, Pshenichnikov MS, Wiersma DA. 1997. *Opt. Lett.* 22:1338–40

8. Scherer NF, Carlson RJ, Matro A, Du M, Ruggiero AJ, et al. 1991. *J. Chem. Phys.* 95:1487–511

9. Albrecht AW, Hybl JD, Faeder SMG, Jonas DM. 2000. *J. Chem. Phys.* In press

10. Pastirk I, Lozovoy VV, Grimberg BI, Brown EJ, Dantus M. 1999. *J. Phys. Chem. A* 103:10226–36

10a. Gallagher SM, Albrecht AW, Hybl JD, Landin BL, Rajaram B, Jonas DM 1998. *J. Opt. Soc. Am. B* 15:2338–345

11. Ernst RR, Bodenhausen G, Wokaun A. 1987. *Principles of Nuclear Magnetic Resonance in One and Two Dimensions.* Oxford, UK: Clarendon

12. Evans JN. 1995. *Biomolecular NMR Spectroscopy.* New York: Oxford Univ. Press

13. Sanders JKM, Hunter BH. 1993. *Modern NMR Spectroscopy.* New York: Oxford Univ. Press

14. Mukamel S. 1990. *Annu. Rev. Phys. Chem.* 41:647–81

15. Loring RF, Mukamel S. 1985. *J. Chem. Phys.* 83:2116

16. Mukamel S, Piryatinski A, Chernyak V. 1999. *Acct. Chem. Res.* 32:145–54

17. Mukamel S, Chemla DS, eds. 1996. *Chem. Phys.* 210:1–388

18. Kobayashi T, ed. 1996. *J-Aggregates.* Singapore: World Sci.

19. Tani T. 1995. *Photographic Sensitivity.* New York: Oxford Univ. Press

20. Hoff AJ, Deisenhofer J. 1997. *Phys. Rep.* 287:2–247

21. Van Grondelle R, Dekker JP, Gillbro T, Sundstrom V. 1994. *Biochim. Biophys. Acta* 1187:1

22. Sundstrom V, Pullerits T, van Grondelle R. 1999. *J. Phys. Chem. B* 103:2327

23. Garab G, ed. 1998. *Photosynthesis: Mechanisms and Effects,* Vols 1–4. Dordrecht, Ger.: Kluwer

24. *J. Phys. Chem. B.* 1997. (Special Issue on Light-Harvesting Physics Workshop.) 101

25. Krimm S, Bandeker J. 1986. *J. Adv. Protein Chem.* 38:181

26. Torii H, Tasumi M. 1992. *J. Chem. Phys.* 96:3379

27. Surewicz WK, Mantch HH, Chapman D. 1993. *Biochemistry* 32:389

27a. Leckson M, Mantsch H. 1995. *Crit. Rev. Biochem. Mol. Biol.* 30:95

28. Hamm P, Lim M, DeGrado WF, Hochstrasser R. 1999. *Proc. Natl. Acad. Sci. USA* 96:2036

29. Hamm P, Lim M, Hochstrasser RM. 1998. *J. Phys. Chem. B* 102:6123

29a. Hamm P, Lim M, Hochstrasser R. 2000. *J. Chem. Phys.* 112:1907

30. Piryatinski A, Chernyak V, Mukamel S. 2000. In *Ultrafast Infrared and Raman Spectroscopy,* ed. MD Fayer. New York: Marcel Dekker. In press

30a. Piryatinski A, Tretiak S, Chernyak V, Mukamel S. 2000 *J. Raman Spectrosc.* 31:125–35

31. Hamm P, Lim M, DeGrado WF, Hochstrasser RM. 1999. *J. Phys. Chem. A* 103:10049

32. Woutersen S, Bakker HJ. 1999. *Phys. Rev. Lett.* 83:2077–88

32a. Nienhuys HK, Woutersen S, Santen RA, Bakker HJ. 1999. *J. Chem. Phys.* 111:1494–500

32b. Woutersen S, Bakker HJ. 1999. *Nature* 402:507

32c. Nitzan A. 1999. *Nature* 402:472

33. Laenen R, Rauscher C, Laubereau A. 1998. *Chem. Phys. Lett.* 283:7–14

34. Gale GM, Gallot G, Hache F, Lascoux N, Bratos S, Leicknan JC. 1999. *Phys. Rev. Lett.* 82:1068–71

35. Jimenez R, Fleming GR, Kumar PV, Maroncelli M. 1994. *Nature* 369:471

36. Laenen R, Rauscher C, Laubereau A. 1998. *Phys. Rev. Lett.* 80:2622

37. Bratos S, Leicknam J-Cl. 1995. *J. Chem. Phys.* 103:4887

38. Chudoba C, Nibbering ETJ, Elsaesser T. 1998. *Phys. Rev. Lett.* 81:3010–13

38a. Chudoba C, Nibbering ETJ, Elsaesser T. 1998. *J. Phys. Chem. A* 103:5625–28

38b. Tschirschwitz F, Nibbering ETJ. 1999. *Chem. Phys. Lett.* 312:169

39. Palese S, Schilling L, Miller RJD, Staver PR, Lotshaw WT. 1994. *J. Phys. Chem.* 98:6308–16

40. Pope M, Swenberg CE. 1999. *Electronic Processes in Organic Crystals and Polymers.* New York: Oxford Univ. Press

41. Silinsh EA, Čápek V. 1994. *Organic Molecular Crystals.* New York: AIP

42. Chernyak V, Zhang WM, Mukamel S. 1999. *J. Chem. Phys.* 109:9587–601

42a. Zhang WM, Chernyak V, Mukamel S. 1999. *J. Chem. Phys.* 110:5011–28

43. Joo T, Jia Y, Yu J-Y, Jonas DM, Fleming GR. 1996. *J. Phys. Chem.* 100:2399

44. Reddy NRS, Picorel R, Small GJ. 1992. *J. Phys. Chem.* 96:9458

44a. Reddy NRS, Cogdell RJ, Zhao L, Small GJ. 1993. *Photochem. Photobiol.* 57:35

45. Bradforth SE, Jimenez R, van Mourik F, van Grondelle R, Fleming GR. 1998. *J. Phys. Chem.* 99:16179.

46. Book LD, Scherer NF. 1999. *J. Chem. Phys.* 111:792

46a. Book LD, Ostafine AE, Ponomarenko N, Norris JR, Scherer NF. 2000 *J. Phys. Chem. B.* In press

47. Arnett DC, Moser CC, Dutton PL, Scherer NF. 1999. *J. Phys. Chem. B* 103:2014

48. Alden RG, Johnson E, Nagarajan V, Parson WW, Law CJ, Cogdell RG. 1997. *J. Phys. Chem. B* 101:4667

49. Wu HM, Savikhin S, Reddy NRS, Kjankowiak R, Cogdell RJ, et al. 1996. *J. Phys. Chem.* 100:12022

50. Clore GM, Gronenborn AM. 1989. *CRC Crit. Rev. Biochem. Mol. Biol.* 24:479–564

51. Wuthrich K. 1986. *NMR of Proteins and Nucleic Acids.* New York: Wiley

51a. Salzmann M, Wider G, Pervushin K, Wuthrich K. 1999. *J. Biol. Mol. NMR* 15:181–84

51b. Wider G, Wuthrich K. 1999. *Curr. Opin. Struct. Biol.* 9:594–601

51c. Glockshuber R, Hornemann S, Riek R, Billeter M, Wider G, et al. 1997. *Mol. Cell. Biol.* pp. 1–25

52. Bax A. 1982. *Two-Dimensional NMR in Liquids.* Ger.: Dortrecht Delft Univ. Press

52a. Cornilescu G, Hu JS, Bax A. 1999. *J. Am. Chem. Soc.* 121:2949–50

52b. Ottiger M, Bax A. 1998. *J. Biomol. NMR* 12:361–72

53. Gemperle C, Aebli G, Schweiger A, Ernst RR. 1990. *J. Magn. Res.* 88:241–56

53a. Hofer P. 1994 *J. Magn. Res.* 111:77–86

53b. Sastry VSS, Polimeno A, Crepeau RH, Freed JH. 1996. *J. Chem. Phys.* 105: 5773–91

54. Harder H, Nicolaisen HW, Dreizler H, Mader H. 1993. *Chem. Phys. Lett.* 214:265–70

54a. Vogelsanger B, Andrist M, Bauder A. 1988. *Chem. Phys. Lett.* 144:180–86

55. Hybl JD, Albrecht AW, Faeder SMG, Jonas DM. 1998. *Chem. Phys. Lett.* 297:307–13

56. Zhang WM, Chernyak V, Mukamel S. 1998. In *Ultrafast Phenomena XI,* ed. T Elsaesser, JG Fujimoto, DA Wiersma, W Zinth, p. 663. New York: Springer

56a. Mukamel S, Zhang WM, Chernyak V. 1998. In *Photosynthesis: Mechanisms and Effects,* ed. G Garab, 1:3. Dordrecht, Ger.: Kluwer

57. Meier T, Chernyak V, Mukamel S. 1997. *J. Chem. Phys.* 107:8759–74

57a. Zhang WM, Meier T, Chernyak V, Mukamel S. 1998. *J. Chem. Phys.* 108:7763–74

58. Chernyak V, Wang N, Mukamel S. 1995. *Phys. Rep.* 263:213–309

59. de Boeij WP, Pshenichnikov MS, Wiersma DA. 1996. *J. Phys. Chem.* 100:11806

60. Yang M, Fleming GR. 1999. *J. Chem. Phys.* 111:27–39

60a. Yang M, Fleming GR. 1999. *J. Chem. Phys.* 110:2983–90

61. Van Nulcurd NAJ, Forge V, Balbach J, Dobson CM. 1998. *Acc. Chem. Res.* 31:773

62. Siders CW, Cavalleri A, Sokolowski-Tinten K, Toth C, Guo T, et al. 1999. *Science.* 286:1340–42

63. Tomov IV, Oulianov DA, Chen P, Rentzepis PM. 1999. *J. Phys. Chem. B* 103:7081–91

63a. Rose-Petruck C, Jimenez R, Guo T, Cavelleri A, Siders CW, et al. 1999 *Nature* 398:310–12

64. Chin AH, Schoenlein RW, Glover TE, Balling P, Leemans WP, Shank CV. 1999. *Phys. Rev. Lett.* 83:336–39

65. Trebino R, DeLong KW, Fittinghoff DN, Sweetser JN, Krumbugel M, et al. 1997. *Rev. Sci. Instrum.* 68:3277–95

66. Chemla DS, Bigot JY, Mycek MA, Weiss S, Schäfer W. 1997. *Phys. Rev.* 50:8439–53

67. Voehringer P, Arnett DC, Yang TS, Scherer NF. 1995. *Chem. Phys. Lett.* 237:387

68. Lepetit L, Joffre M. 1996. *Opt. Lett.* 21:564–66

68a. Lepetit L, Cheriaux G, Joffre M. 1995. *J. Opt. Soc. Am. B* 12:2467–74

68b. Likforman JP, Joffre M, Thierry-Meig V. 1997. *Opt. Lett.* 22:1104–6

69. Payne J. 1994. *J. Quantum. Electron.* 30:2693–97

70. Chang XJ, Cong P, Simon JD. 1995. *J. Phys. Chem.* 99:7857–59

71. Iaconis C, Walmsley IA. 1999. *IEEE J. Quantum. Electron.* 35:501

72. Mukamel S. 1997. *J. Chem. Phys.* 107:4165–171

73. Meier T, Chernyak V, Mukamel S. 1997. *J. Phys. Chem. B* 101:7332–42

73a. Meier T, Zhao Y, Chernyak V, Mukamel S. 1997. *J. Chem. Phys.* 107:3876–93

73b. Zhang WM, Meier T, Chernyak V, Mukamel S. 1998. *Philos. Trans. R. Soc. London Ser. A* 356:405

74. Sauer K, Cogdell RJ, Prince SM, Freer A,

Issacs NW, Scheer H. 1996. *Photochem. Photobiol.* 64:564

75. Berberan-Santos MN, Canceill J, Gratton E, Jullien L, Lehn JM, et al. 1996. *J. Phys. Chem.* 100:15

76. Balzani V, Scandola F. 1991. *Supramolecular Photochemistry.* New York: Harwood

77. Forrest SR. 1997. *Chem. Rev.* 97:1793

78. Balzani V, Campagna S, Denti G, Juris A, Serroni S, Venturi M. 1998. *Acc. Chem. Res.* 31:26

79. Tomalia DA, Naylor AM, Goddard WA. 1990. *Angew. Chem. Int. Edn. Engl.* 29:138

80. Jiang DL, Aida T. 1998. *J. Am. Chem. Soc.* 120:10895

80a. Jiang DL, Aida T. 1997. *Nature* 388: 454

81. Ward JF. 1935. *Rev. Mod. Phys.* 37:1

81a. Orr BJ, Ward JF. 1971. *Mol. Phys.* 20: 513

82. Kanis DR, Ratner MA, Marks TJ. 1994. *Chem. Rev.* 94:195

83. Brédas JL, Adant C, Tackx P, Persoons A, Pierce BM. 1994. *Chem. Rev.* 94:243

84. Spano FC, Mukamel S. 1991. *Phys. Rev. Lett.* 66:1197

84a. Spano FC, Mukamel S. 1991. *J. Chem. Phys.* 95:7526

85. Mukamel S. 1994. In *Molecular Nonlinear Optics,* ed. J Zyss, p. 1–46. New York: Academic

86. Leegwater JA, Mukamel S. 1994. *J. Chem. Phys.* 101:7388

87. Dubovsky O, Mukamel S. 1998. *J. Chem. Phys.* 95:7828

88. Leegwater JA, Mukamel S. 1992. *Phys. Rev. A* 46:452

89. Knoester J, Mukamel S. 1992. *Phys. Rep.* 205:1

90. Kühn O, Chernyak V, Mukamel S. 1996. *J. Chem. Phys.* 105:8586

91. Jenkins J, Mukamel S. 1993. *J. Chem. Phys.* 98:7046–58

91a. Chernyak V, Mukamel S. 1993. *Phys. Rev. B* 48:2470–78

91b. Wagersreiter T, Mukamel S. 1996. *J. Chem. Phys.* 105:7997–8010

92. Louwe RJW, Vrieze J, Hoff AJ, Aartsma TJ. 1997. *J. Phys. Chem. B* 101: 1120

92a. Vulto SIE, deBaat MA, Neerken S, Nowak FR, van Amerongen H, et al. 1999. *J. Phys. Chem. B* 103:8153–61

92b. Vulto SIE, deBaat MA, Louwe RJW, Permentier HP, Neef T, et al. 1998. *J. Phys. Chem. B* 102:9577–82

93. Kuhlbrandt W, Wang DN, Fujiyoshi Y. 1994. *Nature* 367:614

94. Gradinaru CC, Ozdemir S, Gulen D, van Stokkum IHM, van Grondelle R, van Amerongen H. 1998. *Biophys. J.* 75:3064–77

94a. Gradinaru CC, Pascal AA, van Mourik F, Robert B, Horton P, et al. 1998. *Biochemistry* 37:1143

95. Connelly JP, Muller MG, Hucke M, Gatzen G, Mullineaus CW, et al. 1997. *J. Phys. Chem. B* 101:1902

96. Pagano A, Cinque G, Bassi R. 1998. *J. Biol. Chem.* 273:17154

96a. Blankenship RE, Olson JM, Miller M. 1995. In *Anoxygenic Photosynthetic Bacteria*, ed. RE Blankenship, MT Mudigan, CE Baucer, pp. 399–435. Netherlands: Kluwer

97. Economou EN. 1983. *Green's Functions in Quantum Physics.* New York: Springer

98. Mukamel S, Wang HX. 1992. *Phys. Rev. Lett.* 69:65

98a. Mukamel S, Takahashi A, Wang HX, Chen G. 1994. *Science* 266:250

98b. Mukamel S, Tretiak S, Wagersreiter T, Chernyak V. 1997. *Science* 277:781

98c. Tretiak S, Zhang WM, Chernyak V, Mukamel S. 1999. *Proc. Natl. Acad. Sci. USA* 96:13003–8

99. Yokojima S, Meier T, Mukamel S. 1997. *J. Chem. Phys.* 106:3837–53

100. Koolhaas MH, van der Zwan G, Frese RN, van Grondelle R. 1997. *J. Phys. Chem. B* 101:7262

100a. Koolhaas MH, Frese RN, Fowler GJS, Bibby TS, Georgakopoulou S, et al. 1998. *Biochemistry* 37:4693

101. Pullerits T, Chachvisvilis M, Sundstrom V. 1996. *J. Phys. Chem.* 100:10787

102. Chachvisvilis M, Pullerits T, Jones MR, Hunter CN, Sundstrom V. 1997. *J. Phys. Chem. B* 101:7275

103. van Burgel M, Wiersma DA, Duppen K. 1995. *J. Chem. Phys.* 102:20

103a. Durrant JR, Knoester J, Wiersma DA. 1994. *Chem. Phys. Lett.* 222:450

104. Leupold D, Voigt B, Pfeiffer M, Bandilla M, Scheer H. 1993. *Photochem. Photobiol.* 57:24

105. Leupold D, Stiel H, Teuchner K, Nowak F, Sandner W, et al. 1996. *Phys. Rev. Lett.* 77:4675

106. Grad J, Hernandez G, Mukamel S. 1988. *Phys. Rev. A* 37:2835

106a. Spano FC, Mukamel S. 1989. *J. Chem. Phys.* 91:683

106b. Spano FC, Kuklinski JR, Mukamel S. 1990. *J. Phys. Rev. Lett.* 65:211

106c. Mukamel S. 1991. *Chem. Phys.* 94:7534

107. Shahbazyan TV, Raikh ME, Vardney ZV. 2000. *Phys. Rev.* In press

107a. Ozcelik S, Ozcelik I, Akins D. 1998. *Appl. Phys. Lett.* 73:1949

107b. Ozcelik S, Akins D. 1997. *J. Phys. Chem.* 101:3021

108. Dicke RH. 1954. *Phys. Rev.* 93:99.

109. Brandes T, Inoue J, Shimizu A. 1998. *Phys. Rev. Lett.* 80:3952

110. Oberli DY, Vouilloz F, Kapon E. 1997. *Phys. Status Solidi* 164:353

111. Thorne JRG, Williams SA, Hochstrasser, RM, Fagan PJ. 1991. *Chem. Phys.* 157:401

112. Muneter AA, Brumbaugh DV, Apolito J, Horn LA, Spano FC, Mukamel S. 1992. *J. Phys. Chem.* 96:2748

112a. Lanzfame JM, Muneter AA, Brumbaugh DV. 1996. *Chem. Phys.* 210:79

113. Fidder H, Knoester J, Wiersma DA. 1990. *Chem. Phys. Lett.* 171:529

113a. Durrant JR, Knoester J, Wiersma DA. 1992. *Chem. Phys. Lett.* 222:450

114. Monshouwer R, Abrahamsson M, van Mourik F, van Grondelle R. 1997. *J. Phys. Chem. B* 101:7241

115. Zhao Y, Meier T, Zhang W, Chernyak V, Mukamel S. 1999. *J. Phys. Chem.* 103:3954

116. Moerner WE, Orrit M. 1999. *Science* 283:1670

117. Tietz C, Chekhlov O, Drabenstedt A, Schuster J, Wrachtrup J. 1999. *J. Phys. Chem. B* 103:6328–33

118. van Oijen AM, Ketelaars M, Kohler J, Aartsma TJ, Schmidt J. 1998. *J. Phys. Chem. B* 102:9363–66

118a. van Oijen AM, Ketelaars M, Kohler J, Aartsma TJ, Schmidt J. 1999. *Chem. Phys.* 247:53–60

119. Bopp MA, Jia Y, Li L, Cogdell RJ, Hochstrasser RM. 1997. *Proc. Natl. Acad. Sci. USA* 94:10630

119a. Bopp MA, Sytnik S, Howard TD, Cogdell RJ, Hochstrasser RM. 1999. *Proc. Natl. Acad. Sci. USA* 96:1127

120. van Oijen AM, Ketelaars M, Köhler J, Aartsma TJ, Schmidt J. 1998. *J. Phys. Chem. B* 102:9363

121. Hu JY, Barbara PF. 1999. *J. Am. Chem. Soc.* 121:6936–37

122. Chernyak V, Meier T, Tsiper EV, Mukamel S. 2000. *J. Phys. Chem. A* 103:10294–99

123. Nagarajan V, Alden RG, Williams JC, Parson WW. 1996. *Proc. Natl. Acad. Sci. USA* 93:13774

124. Jimenez R, van Mourik F, Fleming GR. 1997. *J. Phys. Chem. B* 101:7350

125. Chernyak V, Minami T, Mukamel S. 2000. *J. Chem. Phys.* 112:7953–63

126. Yan YJ, Mukamel S. 1990. *Phys. Rev. A* 41:6485

126a. Fried LE, Mukamel S. 1993. *Adv. Chem. Phys.* 84:435

127. Pollard WT, Coalson RA. 1994. *J. Chem. Phys.* 100:5054–65

128. Figueirido FE, Levy RM. 1992. *J. Chem. Phys.* 97:703–6

129. Redfield AG. 1969. *Adv. Magn. Reson.* 1:1

130. Jeener J. 1982. *Adv. Magn. Reson.* 10:1–51

131. Weiner AM, DeSilvestri SD, Ippen EP. 1985. *J. Opt. Soc. Am. B* 2:654–61

132. Shoemaker RL, Hopf FA. 1974. *Phys. Rev. Lett.* 33:1527–30

133. Kleiman VD, Arrivo SM, Melinger JS, Heilweil EJ. 1998. *Chem. Phys.* 233:207–16

134. Rector KD, Kwok AS, Ferrante C, Tokmakoff A, Fayer MD. 1997. *J. Chem. Phys.* 106:10027

134a. Rector KD, Fayer MD. 1998. *Int. Rev. Phys. Chem.* 17:261–306

135. Leeson DT, Wiersma DA. 1995. *Phys. Rev. Lett.* 74:2138

135a. Leeson DT, Wiersma DA. 1995. *Nat. Struct. Biol.* 2:848

135b. Hamm P, Lim M, Hochstrasser RM. 1998. *Phys. Rev. Lett.* 81:5326

135c. Lim M, Hamm P, Hochstrasser RM. 1998. *Proc. Natl. Acad. Sci. USA* 95:15315

136. Rella CW, Kwok A, Rector K, Hill JR, Schwettman HA, et al. 1996. *Phys. Rev. Lett.* 77:1648

136a. Hill JR, Dlott DD, Rella CW, Peterson KA, Decatur SM, et al. 1996. *J. Phys. Chem.* 100:15620

136b. Rella CW, Rector K, Kwok A, Hill JR, Schwettman HA, et al. 1996. *J. Phys. Chem.* 100:12100

136c. Rector KD, Engholm JR, Rella CW, Hill JR, Dlott DD, Fayer MD. 1999. *J. Phys. Chem.* 103:2381–87

137. Torii H, Tasumi M. 1993. *J. Chem. Phys.* 99:8459–65

138. Narasimhan LR, Littau KA, Pack DW, Bai YS, Elschner A, Fayer MD. 1990. *Chem. Rev.* 90:439

139. Wright JC. 1997. *Appl. Spectrosc.* 51:949

139a. Zhao W, Wright JC. 2000. *J. Am. Chem. Soc.* 21:10994–98

139b. Zhao W, Wright JC. 1999. *Phys. Rev. Lett.* 83:1950–1953

139c. Zhao W, Wright JC. 2000. *Phys. Rev. Lett.* 84:1411–14

140. Noda I. 1993. *Appl. Spectrosc.* 47:1329

141. Okumura K, Tanimura Y. 1997. *Chem. Phys. Letts.* 278:175–183

141a. Okumura K, Tokmakoff A, Tanimura Y. 1999. *J. Chem. Phys.* 111:492

142. Karplus M. 1997. In *Femtochemistry and Femtobiology: Ultrafast Reaction Dynamics at Atomic-Scale Resolution*, ed. V Sundstrom, pp. 386–422. London: Imperial College Press

142a. Dobson CM, Sali A, Karplus M. 1998. *Angew. Chem. Int. Ed. Engl.* 37:868

142b. Gruebele M, 1999. *Annu. Rev. Phys. Chem.* 50:485–516

143. Valentine JS. 1998. *Acc. Chem. Res.* 31:697–780

144. Chen XG, Li P, Holtz JSW, Chi Z, Pajcini V, et al. 1996. *J. Am. Chem. Soc.* 118:9705

145. Surewicz WK, Mantsch HH. 1988. *Biochim. Biophys. Acta* 952:115

146. Gruebele M, Sabelko J, Ballew R, Ervin J. 1998. *Acc. Chem. Res.* 31:699

147. Phillips CM, Mizutani Y, Hochstrasser RM. 1995. *Proc. Natl. Acad. Sci. USA* 92:7292

148. Williams S, Causgrove TP, Gilmanshin R, Fang KS, Callender RH, et al. 1996. *Biochemistry* 35:691

149. Reinstadler D, Fabian H, Backmann J, Naumann D. 1996. *Biochemistry* 35:15822

150. Dyer RB, Gai F, Woodruff WH, Gilmanshin R, Callender RH. 1998. *Acc. Chem. Res.* 31:709

151. Thompson PA, Eaton WA, Hofziehter J. 1997. *Biochemistry* 36:9200–10

152. Tanimura Y, Mukamel S. 1993. *J. Chem. Phys.* 99:9496–511

153. Blank DA, Kaufman LJ, Fleming GR. 1999. *J. Chem. Phys.* 111:3105

154. Kirkwood JC, Ulness DJ, Albrecht AC. 1999. *J. Chem. Phys.* 111:253–80

154a. Stimson MJ, Ulness DJ, Albrecht AC. 1997. *Chem. Phys.* 222:17

155. Ivanecky JE, Wright JC. 1993. *Chem. Phys. Lett.* 206:437

156. Mukamel S, Khidekel V, Chernyak V. 1996. *Phys. Rev. E.* 53:R1

156a. Mukamel S. 2000. *Phys. Rev. A.* 61:21804–6

157. Shemetulskis NE, Loring RF. 1992. *J. Chem. Phys.* 97:1217

157a. Pentidis SA, Loring RF. 1998. *Chem. Phys. Lett.* 287:217

158. Bernasconi M, Silvestrelli PL, Parrinello M. 1998. *Phys. Rev. Lett.* 81:1235–38

159. Saito S, Ohmine I. 1998. *J. Chem. Phys.* 108:240

160. Sepulveda MA, Mukamel S. 1995. *J. Chem. Phys.* 102:9327–44

161. Mukamel S, Piryatinski A, Chernyak V. 1999. *J. Chem. Phys.* 110:1711–25

162. Meier T, Mukamel S. 1996. *Phys. Rev. Lett.* 77:3471–74

162a. Meier T, Tretiak S, Cherynak V, Mukamel S. 1997. *Phys. Rev. B* 55:4960–77

163. Davidson ER. 1976. *Reduced Density Matrices in Quantum Chemistry.* New York: Academic

163a. Szabo A, Ostlund NA. 1989. *Modern Quantum Chemistry.* New York: McGraw-Hill

164. Gross EKU, Dobson JF, Petersilka M. 1996. In *Density Functional Theory*, ed. RF Nalewajski 181:1–81. Berlin: Springer

165. Casida ME. 1995. In *Recent Advances in Density-Functional Methods*, Part I, ed. DA Chong, 3:155–92. Singapore: World Sci.

166. Davis WB, Svec WA, Ratner MA, Wasielewski MR. 1998. *Nature* 396:60

167. Fiebig T, Wan C, Kelley SO, Barton JK, Zewail AH. 1999. *Proc. Natl. Acad. Sci. USA* 96:1187

168. Scholes GD, Ghiggino KP, Oliver AM, Paddon-Row MN. 1993. *J. Am. Chem. Soc.* 115:4345

168a. Clayton AHA, Scholes GD, Ghiggino KP, Paddon-Row MN. 1996. *J. Phys. Chem.* 100:10912

169. Speiser S. 1996. *Chem. Rev.* 97:1953

170. Jortner J, Bixon M, eds. 1999. *Electron Transfer Adv. Chem. Phys.* 106:107. New York: Wiley

171. Chemla DS, Shah J. 2000. *Proc. Natl. Acad. Sci. USA.* 97:2437–44

171a. Chemla DS. 1999. *Semiconduct. Semimetals* 58:175–256
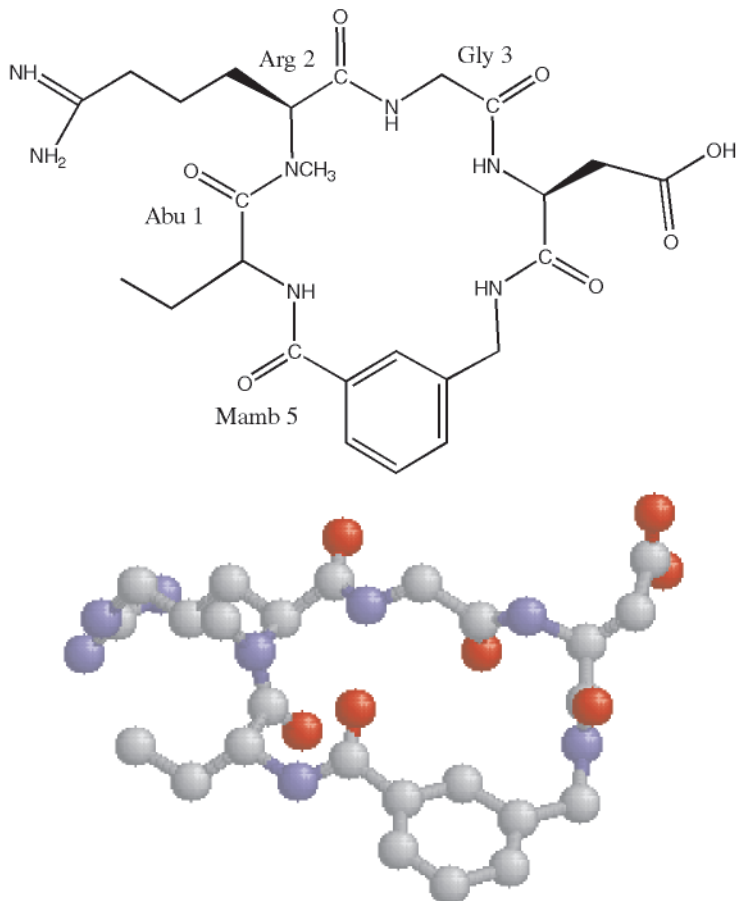
Figure 7 3D structure of the cyclic pentapeptide (172).
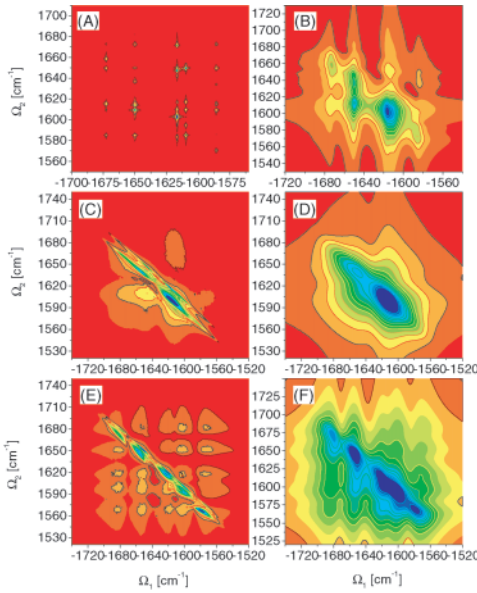
Figure 9 Absolute value $|S(\Omega_2,\Omega_1)|$ of 2D infrared photon echo signal for models (A)–(F). (Different panels have a different color code. Red is zero and maximum is blue.) (30)
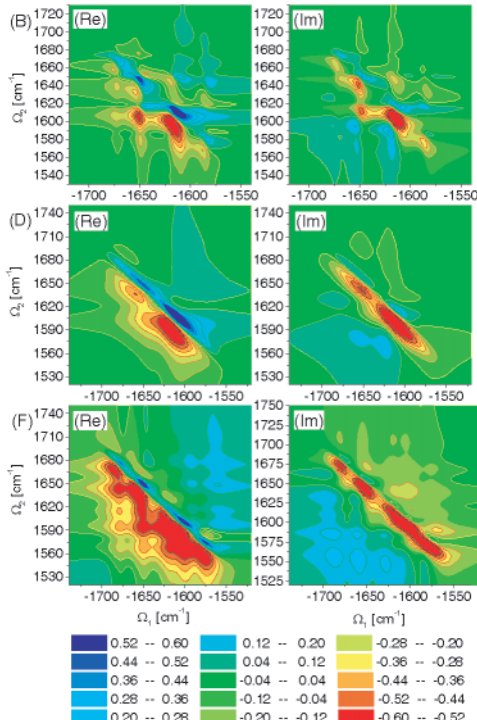
Figure 10 Real and imaginary parts of the 2D signal $S(\Omega_2,\Omega_1)$ for models (B), (D), and (F). (30)